



## Study of the response of the ATLAS central calorimeter to pions of energies from 3 to 9 GeV

E. Abat<sup>a,1</sup>, J.M. Abdallah<sup>b</sup>, T.N. Addy<sup>c</sup>, P. Adragna<sup>d</sup>, M. Aharrouche<sup>e</sup>, A. Ahmad<sup>f</sup>, T.P.A. Akesson<sup>g</sup>, M. Aleksa<sup>h,\*</sup>, C. Alexa<sup>i</sup>, K. Anderson<sup>j</sup>, F. Anghinolfi<sup>h</sup>, A. Antonaki<sup>k</sup>, G. Arabidze<sup>k</sup>, E. Arik<sup>a</sup>, O.K. Baker<sup>l</sup>, D. Banfi<sup>m</sup>, S. Baron<sup>h</sup>, H.P. Beck<sup>n</sup>, B. Belhorma<sup>o</sup>, D. Bencheekroun<sup>p</sup>, D.P. Benjamin<sup>q</sup>, K. Benslama<sup>r</sup>, E. Bergeaas Kuutmann<sup>s</sup>, H. Bertelsen<sup>t</sup>, S. Binet<sup>u</sup>, C. Biscarat<sup>v</sup>, V. Boldea<sup>i</sup>, V.G. Bondarenko<sup>w</sup>, M. Boonekamp<sup>x</sup>, M. Bosman<sup>b</sup>, C. Bourdarios<sup>u</sup>, D. Burckhart Chromek<sup>h</sup>, V. Bychkov<sup>y</sup>, J. Callahan<sup>z</sup>, D. Calvet<sup>aa</sup>, M. Canneri<sup>ab</sup>, M. Capeáns Garrido<sup>h</sup>, M. Caprini<sup>i</sup>, L. Cardiel Sas<sup>h</sup>, T. Carli<sup>h</sup>, L. Carminati<sup>m</sup>, J. Carvalho<sup>ac</sup>, M. Cascella<sup>ab</sup>, M.V. Castillo<sup>ad</sup>, A. Catinaccio<sup>h</sup>, M. Cavalli Sforza<sup>b</sup>, D. Cavalli<sup>ae</sup>, V. Cavasinni<sup>ab</sup>, S.A. Cetin<sup>a</sup>, H. Chen<sup>af</sup>, R. Cherkaoui<sup>ag</sup>, F. Chevallier<sup>o</sup>, M. Ciobotaru<sup>ah</sup>, M. Citterio<sup>ae</sup>, B. Cleland<sup>ai</sup>, E. Cogneras<sup>n</sup>, P. Conde Muino<sup>ac</sup>, M. Consonni<sup>m</sup>, S. Constantinescu<sup>i</sup>, T. Cornelissen<sup>h</sup>, A. Corso Radu<sup>h</sup>, G. Costa<sup>ae</sup>, P. Cwetanski<sup>z</sup>, D. Da Silva<sup>aj</sup>, M. Dam<sup>h</sup>, H.O. Danielsson<sup>h</sup>, D. Dannheim<sup>h</sup>, T. Davidek<sup>ak</sup>, K. De<sup>al</sup>, P.O. Defay<sup>aa</sup>, B. Dekhissi<sup>am</sup>, J. Del Peso<sup>an</sup>, M. Delmastro<sup>h</sup>, T. Del Prete<sup>ab</sup>, F. Derue<sup>ao</sup>, L. Di Ciaccio<sup>ap</sup>, B. Di Girolamo<sup>h</sup>, S. Dita<sup>i</sup>, F. Dittus<sup>h</sup>, F. Djama<sup>aq</sup>, T. Djobava<sup>ar</sup>, M. Dobson<sup>h</sup>, B.A. Dolgoshein<sup>w</sup>, A. Dotti<sup>ab</sup>, G. Drake<sup>as</sup>, N. Dressnandt<sup>at</sup>, C. Driouchi<sup>t</sup>, W.L. Ebenstein<sup>q</sup>, P. Eerola<sup>g</sup>, I. Efthymiopoulos<sup>h</sup>, K. Egorov<sup>z</sup>, T.F. Eifert<sup>h</sup>, M. El Kacimi<sup>au</sup>, A.I. Etievre<sup>x</sup>, A. Fabich<sup>h</sup>, A.I. Fakhir-Edine<sup>av</sup>, M. Fanti<sup>m</sup>, A. Farbin<sup>al</sup>, P. Farthouat<sup>h</sup>, D. Fassouliotis<sup>k</sup>, L. Fayard<sup>u</sup>, R. Febbraro<sup>aa</sup>, O.L. Fedin<sup>aw</sup>, A. Fenyuk<sup>ax</sup>, R. Ferrari<sup>ay</sup>, B.C. Ferreira<sup>aj</sup>, A. Ferrer<sup>ad</sup>, G. Filippini<sup>aa</sup>, D. Fournier<sup>u</sup>, P. Francavilla<sup>ab</sup>, D. Francis<sup>h</sup>, R. Froeschl<sup>h</sup>, D. Froidevaux<sup>h</sup>, E. Fullana<sup>as</sup>, S. Gadomski<sup>az</sup>, P. Gagnon<sup>z</sup>, S. Gameiro<sup>h</sup>, R. Garcia<sup>an</sup>, N. Ghodbane<sup>aa</sup>, V. Giakoumopoulou<sup>k</sup>, V. Giangiobbe<sup>ab</sup>, N. Giokaris<sup>k</sup>, G. Glonti<sup>y</sup>, N. Gollub<sup>h</sup>, A. Gomes<sup>ac</sup>, M.D. Gomez<sup>az</sup>, B. Gorini<sup>h</sup>, D. Goujdami<sup>av</sup>, K.J. Grahn<sup>ba</sup>, P. Grenier<sup>bb</sup>, N. Grigalashvili<sup>y</sup>, Y. Grishkevich<sup>bc</sup>, M. Gruwe<sup>h</sup>, C. Guicheney<sup>aa</sup>, A. Gupta<sup>j</sup>, C. Haerberli<sup>n</sup>, Z. Hajduk<sup>bd</sup>, H. Hakobyan<sup>be</sup>, M. Hance<sup>at</sup>, P.H. Hansen<sup>t</sup>, A. Harvey Jr.<sup>c</sup>, A. Henriques Correia<sup>h</sup>, L. Hervas<sup>h</sup>, E. Higon<sup>ad</sup>, J. Hoffman<sup>bf</sup>, J.Y. Hostachy<sup>o</sup>, I. Hruska<sup>ak</sup>, F. Hubaut<sup>aq</sup>, W. Hulsbergen<sup>h</sup>, M. Hurwitz<sup>j</sup>, L. Iconomidou-Fayard<sup>u</sup>, I. Jen-La Plante<sup>j</sup>, P.D.C. Johansson<sup>bg</sup>, K. Jon-And<sup>s</sup>, M. Joos<sup>h</sup>, S. Jorgensen<sup>b</sup>, A. Kaczmarska<sup>ao</sup>, M. Kado<sup>u</sup>, A. Karyukhin<sup>ax</sup>, M. Kataoka<sup>h</sup>, F. Kayumov<sup>bh</sup>, A. Kazarov<sup>aw</sup>, P.T. Keener<sup>at</sup>, G.D. Kekelidze<sup>y</sup>, N. Kerschen<sup>bg</sup>, G. Khoriauli<sup>y</sup>, E. Khramov<sup>y</sup>, A. Khristachev<sup>aw</sup>, J. Khubua<sup>y</sup>, T.H. Kittelmann<sup>ai</sup>, E. Klinkby<sup>q</sup>, T. Koffas<sup>h</sup>, S. Kolos<sup>ah</sup>, S.P. Konovalov<sup>bh</sup>, S. Kopikov<sup>ax</sup>, I. Korolkov<sup>b</sup>, S. Kovalenko<sup>aw</sup>, T.Z. Kowalski<sup>bi</sup>, K. Krüger<sup>h</sup>, V. Kramarenko<sup>bc</sup>, L.G. Kudin<sup>aw</sup>, Y. Kulchitsky<sup>bj</sup>, R. Lafaye<sup>ap</sup>, B. Laforge<sup>ao</sup>, W. Lampl<sup>bk</sup>, F. Lanni<sup>af</sup>, S. Laplace<sup>ap</sup>, A.C. Le Bihan<sup>h</sup>, M. Lechowski<sup>u</sup>, F. Ledroit-Guillon<sup>o</sup>, G. Lehmann<sup>h</sup>, R. Leitner<sup>ak</sup>, D. Lelas<sup>u</sup>, Z. Liang<sup>bf</sup>, Z. Liang<sup>bl,bm</sup>, P. Lichard<sup>h</sup>, M. Lokajicek<sup>bn</sup>, L. Louchard<sup>aa</sup>, K. Loureiro<sup>bo</sup>, A. Lucotte<sup>o</sup>, F. Luehring<sup>z</sup>, B. Lundberg<sup>g</sup>, B. Lund-Jensen<sup>ba</sup>, H. Ma<sup>af</sup>, R. Mackeprang<sup>h</sup>, A. Maio<sup>ac</sup>, V.P. Maleev<sup>aw</sup>, F. Malek<sup>o</sup>, J. Maneira<sup>ac</sup>, L. Mandelli<sup>m</sup>, M. Mazzanti<sup>ae</sup>, A. Manousakis<sup>k</sup>, L. Mapelli<sup>h</sup>, C. Marques<sup>ac</sup>, F. Martin<sup>at</sup>, M. Mazzanti<sup>ae</sup>, K.W. McFarlane<sup>c</sup>, G. Mchedlidze<sup>ar</sup>, R. McPherson<sup>bp</sup>, C. Meirosu<sup>h</sup>, Z. Meng<sup>bq,br</sup>, A. Miagkov<sup>ax</sup>, V. Mialkovski<sup>y</sup>, D. Milstead<sup>s</sup>, I. Minashvili<sup>y</sup>, B. Mindur<sup>bi</sup>, V.A. Mitsou<sup>ad</sup>, E. Monnier<sup>aq</sup>, S.V. Morozov<sup>w</sup>, M. Mosidze<sup>ar</sup>, S.V. Mouraviev<sup>bh</sup>, A. Munar<sup>at</sup>, A.V. Nadtochi<sup>aw</sup>, A. Negri<sup>ay</sup>, S. Nemecek<sup>bn</sup>, M. Nessi<sup>h</sup>, S.Y. Nesterov<sup>aw</sup>, F.M. Newcomer<sup>at</sup>, I. Nikitine<sup>ax</sup>, I. Nikolic-Audit<sup>ao</sup>, H. Ogren<sup>z</sup>, S.H. Oh<sup>q</sup>, S.B. Oleshko<sup>aw</sup>, J. Olszowska<sup>bd</sup>, A. Onofre<sup>ac</sup>, C. Padilla Aranda<sup>h</sup>, S. Paganis<sup>bg</sup>, D. Pallin<sup>aa</sup>, D. Pantea<sup>i</sup>, V. Paolone<sup>ai</sup>, J. Parsons<sup>bs</sup>, E. Pasqualucci<sup>bt</sup>, M.S. Passmore<sup>h</sup>, S. Patrichev<sup>aw</sup>, M. Pez<sup>an</sup>,

\* Corresponding author.

<sup>1</sup> Deceased.

V. Perez Reale<sup>bs</sup>, L. Perini<sup>ae</sup>, V.D. Peshekhonov<sup>y</sup>, J. Petersen<sup>h</sup>, T.C. Petersen<sup>h</sup>, R. Petti<sup>bu</sup>, J. Pilcher<sup>j</sup>, J. Pina<sup>bv</sup>, B. Pinto<sup>bv</sup>, F. Podlyski<sup>aa</sup>, L. Poggioli<sup>u</sup>, J. Poveda<sup>bw</sup>, P. Pralavorio<sup>aq</sup>, L. Pribyl<sup>h</sup>, M.J. Price<sup>h</sup>, D. Prieur<sup>bx</sup>, C. Puigdengoles<sup>b</sup>, P. Puzo<sup>u</sup>, S. Rajagopalan<sup>af</sup>, C. Rembser<sup>h</sup>, M. Ridel<sup>ao</sup>, I. Riu<sup>az</sup>, C. Roda<sup>ab</sup>, O. Rohne<sup>by</sup>, A. Romaniouk<sup>w</sup>, D. Rousseau<sup>u</sup>, A. Ruiz<sup>ad</sup>, N. Rusakovich<sup>y</sup>, D. Rust<sup>z</sup>, Y.F. Ryabov<sup>aw</sup>, V. Ryjov<sup>y</sup>, O. Salto<sup>b</sup>, B. Salvachua<sup>as</sup>, C. Santamarina Rios<sup>h</sup>, C. Santoni<sup>aa</sup>, J.G. Saraiva<sup>ac</sup>, F. Sarri<sup>ab</sup>, G. Sauvage<sup>ap</sup>, L.P. SAYS<sup>aa</sup>, M. Schaefer<sup>o</sup>, V.A. Schegelsky<sup>aw</sup>, G. Schlager<sup>h</sup>, J. Schlereth<sup>as</sup>, C. Schmitt<sup>bz</sup>, P. Schwemling<sup>ao</sup>, J. Schwindling<sup>x</sup>, J.M. Seixas<sup>aj</sup>, D.M. Seliverstov<sup>aw</sup>, L. Serin<sup>u</sup>, N. Shalanda<sup>ca</sup>, T. Shin<sup>c</sup>, A. Shmeleva<sup>bh</sup>, J. Silva<sup>ac</sup>, S. Simion<sup>u</sup>, M. Simonyan<sup>ap</sup>, J.E. Sloper<sup>h</sup>, S.Yu. Smirnov<sup>w</sup>, L. Smirnova<sup>bc</sup>, C. Solans<sup>ad</sup>, A. Solodkov<sup>ax</sup>, O. Solovianov<sup>ax</sup>, I. Soloviev<sup>aw</sup>, V.V. Sosnovtsev<sup>w</sup>, F. Spanò<sup>bs</sup>, P. Speckmeyer<sup>h</sup>, S. Stancu<sup>ah</sup>, R. Stanek<sup>as</sup>, E. Starchenko<sup>ax</sup>, A. Straessner<sup>cb</sup>, S.I. Suchkov<sup>w</sup>, M. Suk<sup>ak</sup>, R.R. Szczygiel<sup>bd</sup>, F. Tarrade<sup>af</sup>, F. Tartarelli<sup>ae</sup>, P. Tas<sup>ak</sup>, Y. Tayalati<sup>aa</sup>, R. Teuscher<sup>cc</sup>, M. Thioye<sup>f</sup>, V.O. Tikhomirov<sup>bh</sup>, S. Tisserant<sup>aq</sup>, L. Tremblet<sup>h</sup>, P. Tsiarehka<sup>bj</sup>, G. Unal<sup>h</sup>, G. Unel<sup>z</sup>, G. Usai<sup>j</sup>, A. Valero<sup>ad</sup>, S. Valkar<sup>ak</sup>, J.A. Valls<sup>ad</sup>, R. Van Berg<sup>at</sup>, W. Vandelli<sup>h</sup>, F. Vannucci<sup>ao</sup>, A. Vartapetian<sup>al</sup>, V.I. Vassilikopoulos<sup>c</sup>, L. Vassilieva<sup>bh</sup>, F. Vazeille<sup>aa</sup>, Y. Vetter-Cole<sup>bf</sup>, I. Vichou<sup>cd</sup>, V. Vinogradov<sup>y</sup>, I. Vivarelli<sup>ab</sup>, M. Volpi<sup>b</sup>, C. Wang<sup>q</sup>, P. Werner<sup>h</sup>, S. Wheeler<sup>ce</sup>, M. Wiesmann<sup>h</sup>, H. Wilkens<sup>h</sup>, H.H. Williams<sup>at</sup>, I. Wingerter-Seez<sup>ap</sup>, Y. Yasu<sup>cf</sup>, A. Zaitsev<sup>ax</sup>, A. Zenin<sup>ax</sup>, T. Zenis<sup>cg</sup>, Z. Zenonos<sup>ab</sup>, H. Zhang<sup>aq</sup>, N. Zhou<sup>bs</sup>

<sup>a</sup> Bogazici University, Faculty of Sciences, Department of Physics, TR - 80815 Bebek-Istanbul, Turkey

<sup>b</sup> Institut de Física d'Altes Energies, IFAE, Universitat Autònoma de Barcelona, Edifici Cn, ES - 08193 Bellaterra, Barcelona, Spain

<sup>c</sup> Hampton University, Department of Physics, Hampton VA 23668, United States

<sup>d</sup> Queen Mary, University of London, Mile End Road, E1 4NS London, United Kingdom

<sup>e</sup> Universität Mainz, Institut fuer Physik, Staudinger Weg 7, DE 55099, Germany

<sup>f</sup> Department of Physics and Astronomy, Stony Brook, NY 11794-3800, United States

<sup>g</sup> Lunds universitet, Naturvetenskapliga fakulteten, Fysiska institutionen, Box 118, SE - 221 00, Lund, Sweden

<sup>h</sup> European Laboratory for Particle Physics (CERN), CH-1211 Geneva 23, Switzerland

<sup>i</sup> National Institute of Physics and Nuclear Engineering (Bucharest -IFIN-HH), P.O. Box MG-6, R-077125 Bucharest, Romania

<sup>j</sup> University of Chicago, Enrico Fermi Institute, 5640 S. Ellis Avenue, Chicago, IL 60637, United States

<sup>k</sup> University of Athens, Nuclear & Particle Physics Department of Physics, Panepistimiopoli Zografou, GR 15771 Athens, Greece

<sup>l</sup> Yale University, Department of Physics, PO Box 208121, New Haven, CT06520-8121, United States

<sup>m</sup> Università di Milano, Dipartimento di Fisica and INFN, via Celoria 16, IT - 20133 Milano, Italy

<sup>n</sup> University of Bern, Laboratory for High Energy Physics, Sidlerstrasse 5, CH - 3012 Bern, Switzerland

<sup>o</sup> Laboratoire de Physique Subatomique et de Cosmologie CNRS/IN2P3, Université Joseph Fourier INPC, 53 avenue des Martyrs, FR - 38026 Grenoble Cedex, France

<sup>p</sup> Université Hassan II, Faculté des Sciences Ain Chock, B.P. 5366, MA - Casablanca, Morocco

<sup>q</sup> Duke University, Department of Physics Durham, NC 27708, United States

<sup>r</sup> University of Regina, Physics Department, Canada

<sup>s</sup> Stockholm University, Department of Physics, SE - 106 91 Stockholm, Sweden

<sup>t</sup> University of Copenhagen, Niels Bohr Institute, Blegdamsvej 17, DK - 2100 Kobenhavn 0, Denmark

<sup>u</sup> LAL, Université Paris-Sud, IN2P3/CNRS, Orsay, France

<sup>v</sup> Centre de Calcul CNRS/IN2P3, Lyon, France

<sup>w</sup> Moscow Engineering & Physics Institute (MEPhI), Kashirskoe Shosse 31, RU 115409 Moscow, Russia

<sup>x</sup> Commissariat à l'Energie Atomique (CEA), DSM/DAPNIA, Centre d'Etudes de Saclay, 91191 Gif-sur-Yvette, France

<sup>y</sup> Joint Institute for Nuclear Research, JINR Dubna, RU - 141 980 Moscow Region, Russia

<sup>z</sup> Indiana University, Department of Physics, Swain Hall West 117, Bloomington, IN 47405-7105, United States

<sup>aa</sup> Laboratoire de Physique Corpusculaire (LPC), IN2P3-CNRS, Université Blaise-Pascal Clermont-Ferrand, FR - 63177 Aubiere, France

<sup>ab</sup> Università di Pisa, Dipartimento di Fisica E. Fermi and INFN Pisa, Largo B.Pontecorvo 3, IT - 56127 Pisa, Italy

<sup>ac</sup> Laboratório de Instrumentação e Física Experimental de Partículas, LIP, Avenida Elias Garcia 14-1, PT - 1000-149 Lisboa, Portugal

<sup>ad</sup> University of Valencia, Centro Mixto UVEG-CSIC, Instituto de Física Corpuscular (IFIC), Apdo. 22085 ES-46071 Spain

<sup>ae</sup> INFN Sezione di Milano, via Celoria 16, IT - 20133 Milano, Italy

<sup>af</sup> Brookhaven National Laboratory, Physics Department, Bldg. 510A Upton S, NY 11973, United States

<sup>ag</sup> Université Mohammed V, Faculté des Sciences, BP 1014, MO - Rabat, Morocco

<sup>ah</sup> University of California, Department of Physics & Astronomy, Irvine, CA 92697-4575, United States

<sup>ai</sup> University of Pittsburgh, Department of Physics and Astronomy, 3941 O'Hara Street, Pittsburgh, PA 15260, United States

<sup>aj</sup> Universidade Federal do Rio De Janeiro, Instituto de Física, Caixa Postal 68528, Ilha do Fundao, BR - 21945-970 Rio de Janeiro, Brazil

<sup>ak</sup> Charles University in Prague, Faculty of Mathematics and Physics, Institute of Particle and Nuclear Physics, V Holesovickach 2, CZ - 18000 Praha 8, Czech Republic

<sup>al</sup> University of Texas at Arlington, Department of Physics, Box 19059, Arlington, TX 76019, United States

<sup>am</sup> Laboratoire de Physique Théorique et de Physique des Particules, Université Mohammed Premier, Oujda, Morocco

<sup>an</sup> Universidad Autonoma de Madrid, Facultad de Ciencias, Departamento de Física Teórica, ES - 28049 Madrid, Spain

<sup>ao</sup> Université Pierre et Marie Curie (Paris 6) and Université Denis Diderot (Paris-7), Laboratoire de Physique Nucléaire et de Hautes Energies, CNRS/IN2P3, Tour 33 4 place Jussieu, FR - 75252 Paris Cedex 05, France

<sup>ap</sup> Laboratoire de Physique de Particules (LAPP), Université de Savoie, CNRS/IN2P3, Annecy-le-Vieux Cedex, France

<sup>aq</sup> Université Méditerranée, Centre de Physique des Particules de Marseille, CNRS/IN2P3, F-13288 Marseille, France

<sup>ar</sup> Tbilisi State University, High Energy Physics Institute, University St. 9, GE - 380086 Tbilisi, Georgia

<sup>as</sup> Argonne National Laboratory, High Energy Physics Division, 9700 S. Cass Avenue, Argonne IL 60439, United States

<sup>at</sup> University of Pennsylvania, Department of Physics, High Energy Physics, 209 S. 33rd Street Philadelphia, PA 19104, United States

<sup>au</sup> Laboratoire de Physique de Particules (LAPP), Université de Savoie, CNRS/IN2P3, Annecy-le-Vieux Cedex, France and Université Cadi Ayyad, Marrakech, Morocco

<sup>av</sup> Université Cadi Ayyad, Marrakech, Morocco

<sup>aw</sup> Petersburg Nuclear Physics Institute, RU - 188 300 Gatchina, Russia

<sup>ax</sup> Institute for High Energy Physics (IHEP), Federal Agency of Atom. Energy, Moscow Region, RU - 142 284 Protvino, Russia

<sup>ay</sup> Università di Pavia, Dipartimento di Fisica Nucleare e Teorica and INFN Pavia, Via Bassi 6 IT-27100 Pavia, Italy

<sup>az</sup> Université de Genève, Section de Physique, 24 rue Ernest Ansermet, CH - 1211 Genève 4, Switzerland

<sup>ba</sup> Royal Institute of Technology (KTH), Physics Department, SE - 106 91 Stockholm, Sweden

<sup>bb</sup> SLAC National Accelerator Laboratory, Stanford, CA 94309, United States

- <sup>bc</sup> Lomonosov Moscow State University, Skobeltsyn Institute of Nuclear Physics, RU - 119 991 GSP-1 Moscow Lenskiegory 1-2, Russia
- <sup>bd</sup> The Henryk Niewodniczanski Institute of Nuclear Physics, Polish Academy of Sciences, ul. Radzikowskiego 152, PL - 31342 Krakow Poland
- <sup>be</sup> Yerevan Physics Institute, Alikhanian Brothers Street 2, AM - 375036, Yerevan, Armenia
- <sup>bf</sup> Southern Methodist University, Physics Department, 106 Fondren Science Building, Dallas, TX 75275-0175, United States
- <sup>bg</sup> University of Sheffield, Department of Physics & Astronomy, Hounsfield Road, Sheffield S3 7RH, United Kingdom
- <sup>bh</sup> P.N. Lebedev Institute of Physics, Academy of Sciences, Leninsky pr. 53, RU - 117 924, Moscow, Russia
- <sup>bi</sup> University of Science and Technology, Faculty of Physics and Applied Computer Science of (FPACS AGH-UST), al. Mickiewicza 30, PL-30059 Cracow, Poland
- <sup>bj</sup> B.I. Stepanov Institute of Physics, National Academy of Sciences of Belarus, Independence Avenue 68, Minsk 220072, Republic of Belarus and Joint Institute for Nuclear Research, JINR Dubna, RU - 141 980 Moscow Region, Russia
- <sup>bk</sup> University of Arizona, Department of Physics, Tucson, AZ 85721, United States
- <sup>bl</sup> Institute of Physics, Academia Sinica, TW - Taipei 11529, Taiwan
- <sup>bm</sup> Sun Yat-sen University, School of Physics and Engineering, Guangzhou 510275, PR China
- <sup>bn</sup> Academy of Sciences of the Czech Republic, Institute of Physics and Institute for Computer Science, Na Slovance 2, CZ - 18221 Praha 8, Czech Republic
- <sup>bo</sup> Ohio State University, 191 West Woodruff Ave, Columbus, OH 43210-1117, United States
- <sup>bp</sup> University of Victoria, Department of Physics and Astronomy, P.O. Box 3055, Victoria B.C., Canada V8W 3P6
- <sup>bq</sup> Institute of Physics, Academia Sinica, TW - Taipei 11529, Taiwan
- <sup>br</sup> Shandong University, School of Physics, Jinan, Shandong 250100, PR China
- <sup>bs</sup> Columbia University, Nevis Laboratory, 136 So. Broadway, Irvington, NY 10533, United States
- <sup>bt</sup> Università La Sapienza, Dipartimento di Fisica and INFN Roma 1, Piazzale A. Moro 2, IT- 00185 Roma, Italy
- <sup>bu</sup> University of South Carolina, Columbia, United States
- <sup>bv</sup> LIP and IDMEC-IST, Lisboa, Portugal
- <sup>bw</sup> University of Wisconsin, Department of Physics, 1150 University Avenue, Madison, WI 53706, United States
- <sup>bx</sup> Rutherford Appleton Laboratory, Science and Technology Facilities Council, Harwell Science and Innovation Campus, Didcot OX11 0QX, United Kingdom
- <sup>by</sup> University of Oslo, Department of Physics, P.O. Box 1048, Blindern T, NO - 0316 Oslo, Norway
- <sup>bz</sup> University of Bonn, Physikalisches Institut, Nussallee 12, D - 53115 Bonn, Germany
- <sup>ca</sup> B.I. Stepanov Institute of Physics, National Academy of Sciences of Belarus, Independence Avenue 68, Minsk 220072, Republic of Belarus
- <sup>cb</sup> Technical University Dresden, Institut fuer Kern- und Teilchenphysik, Zellescher Weg 19, D-01069 Dresden, Germany
- <sup>cc</sup> University of Toronto, Department of Physics, 60 Saint George Street, Toronto, Ontario, Canada M5S 1A7
- <sup>cd</sup> University of Illinois, Department of Physics, 1110 West Green Street, Urbana, IL 61801, United States
- <sup>ce</sup> University of Alberta, Department of Physics, Centre for Particle Physics, Edmonton, AB, Canada T6G 2G7
- <sup>cf</sup> KEK, High Energy Accelerator Research Organization, 1-1 Oho Tsukuba-shi, Ibaraki-ken 305-0801, Japan
- <sup>cg</sup> Comenius University, Faculty of Mathematics Physics & Informatics, Mlynska dolina F2, SK - 84248 Bratislava, Slovak Republic

## ARTICLE INFO

### Article history:

Received 11 May 2009

Accepted 12 May 2009

Available online 13 June 2009

### Keywords:

ATLAS  
Calorimetry  
Test beam  
Calibration  
Simulation

## ABSTRACT

A fully instrumented slice of the ATLAS central detector was exposed to test beams from the SPS (Super Proton Synchrotron) at CERN in 2004. In this paper, the response of the central calorimeters to pions with energies in the range between 3 and 9 GeV is presented. The linearity and the resolution of the combined calorimetry (electromagnetic and hadronic calorimeters) was measured and compared to the prediction of a detector simulation program using the toolkit Geant 4.

© 2009 Elsevier B.V. All rights reserved.

## 1. Introduction

In 2004 a Combined Test Beam (CTB) program was carried out in the H8 beam line at CERN. A slice of the ATLAS detector composed of the final versions of all central sub-detectors was exposed to the SPS (Super Proton Synchrotron) beam. The layout of the sub-detectors was designed to be as close as possible to the ATLAS layout. The Data Acquisition (DAQ) system [1] was also similar to the one being used in ATLAS.

The calorimeters in ATLAS will be used to measure the energy of jets over a wide energy range from 20 GeV to more than 1 TeV. A large part of the 2004 CTB program was dedicated to low-energy data-taking. This program was particularly important from the point of view of calorimetry since a large fraction of jet energy is carried by particles of few GeV. For example, in a 150 GeV jet, particles with energy smaller than 10 GeV carry about 25% of the total energy [2].

In this paper, the measurement of the response of the central electromagnetic (LAr) and hadronic (TileCal) calorimeters to Very Low-Energy (VLE) pion beams is presented. The response was studied for nominal beam energies of  $3 \leq E_{nom} \leq 9$  GeV and for various incident angles corresponding to pseudo-rapidities of  $\eta_{beam} = 0.20, 0.25, 0.35, 0.45, 0.55$  and  $0.65$ . Particular care was

given to the selection of a clean pion sample and to correcting for any remaining contamination. No corrections for dead material, containment and non-compensation effects were applied in the energy determination. The measured pion response was then compared to the predictions of a Monte Carlo (MC) simulation program [3,4]. The agreement between the data and the simulation is discussed.

## 2. The experimental setup

### 2.1. The beam line

In the SPS H8 line, the very low-energy pion beam is produced by an 80 GeV secondary pion beam impinging on a 1 m-long polyethylene target [5]. The target is a cylinder with a diameter of 4 cm and is placed about 45 m upstream of the detectors (see Fig. 1). An absorber (beam dump) is placed after the target to stop secondary particles with a small deflection angle.

Fig. 1 shows the instrumentation of the beam line upstream of the detectors. There are four dipole magnets (B1, B2, B3 and B4) that perform the momentum and charge selection of VLE particles. Negative pions were selected for the data samples

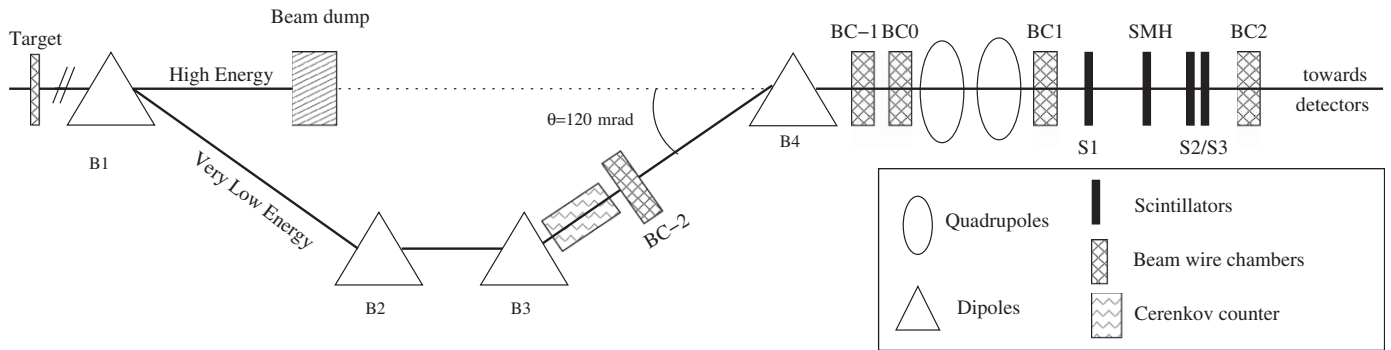


Fig. 1. Schematic layout (not to scale) of the H8 beam line. Only the devices used in this analysis are shown.

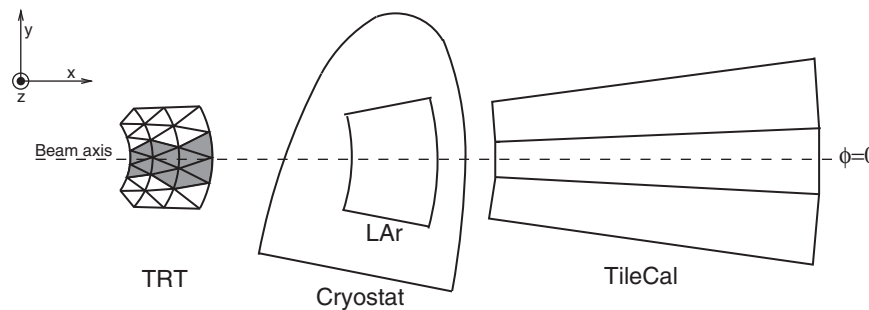


Fig. 2. Side view of the detector layout in the 2004 combined test beam. Only sub-detectors that are used in this paper are represented.

discussed in this paper. A threshold Cherenkov counter  $C$  [6] between  $B3$  and  $B4$  allows the separation of electrons from pions and muons. The transverse beam profile is monitored by five wire chambers [7] ( $BC-2$  to  $BC2$ ). Two scintillators  $S2$  and  $S3$ , with an active surface of  $5 \times 5 \text{ cm}^2$  [8] were used in coincidence to trigger the data acquisition and to provide the trigger timing.

The VLE beam is expected to have the following composition:

- pions with a momentum between 3 and 9 GeV (selected by setting the currents of the magnets  $B1$ – $B4$ ),
- electrons with the same momentum as pions,
- high-energy muons which did not stop in the absorber (halo muons). These muons are not expected to be synchronous with the trigger of the data acquisition.
- low-energy muons coming from meson decays. Their momentum is less than or equal to the momentum of the initial mesons.

In this paper a right-handed coordinate system with the  $x$ -axis along the beam line and  $y$ -axis pointing up is used.

## 2.2. The detector

Fig. 2 shows a side view of the layout of the ATLAS sub-detectors during the 2004 CTB. Only sub-detectors that were used in the present analysis are shown.

The silicon pixel detector, the SemiConductor Tracker (SCT) and the Transition Radiation Tracker (TRT), the three subsystems of the ATLAS inner detector [9], were present in the beam line. Only the TRT information has been used in this analysis. Two barrel modules of the TRT were placed in front of the calorimeters (see Fig. 2). These modules are composed of layers of straws filled with an active gas<sup>2</sup> (each straw acting as a drift chamber), surrounded by a radiator. The readout electronics is designed to provide two

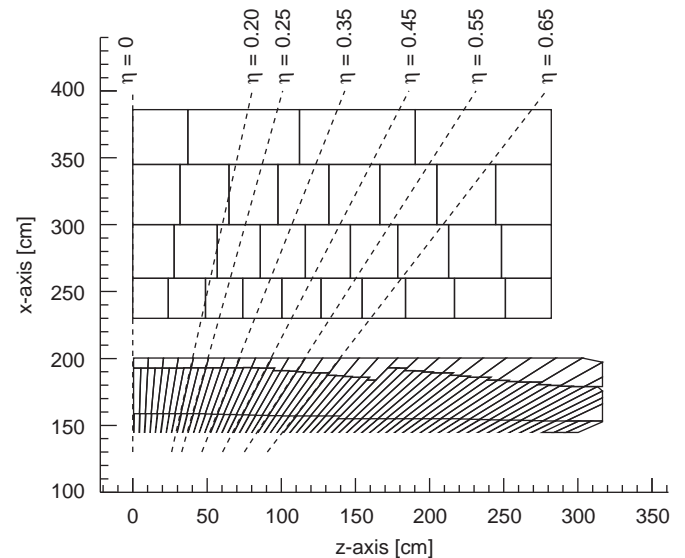


Fig. 3. Top view of the calorimetry layout in the 2004 combined test beam. The TileCal modules are only represented for  $\eta > 0$ .

types of digital signals, depending on the amplitude of the analog signal from the straws:

- a Low-Threshold (LT) signal for tracking hits (a track is defined by 25 LT hits),
- a High-Threshold (HT) signal for energetic photons produced by transition radiation from electrons [9].

A particle passing through the TRT can be identified as an electron or a pion, depending on the number of HT hits recorded along its track. In the study presented in this paper, the TRT information

<sup>2</sup> 70% Xe, 20% CF<sub>4</sub>, 10% CO<sub>2</sub>.

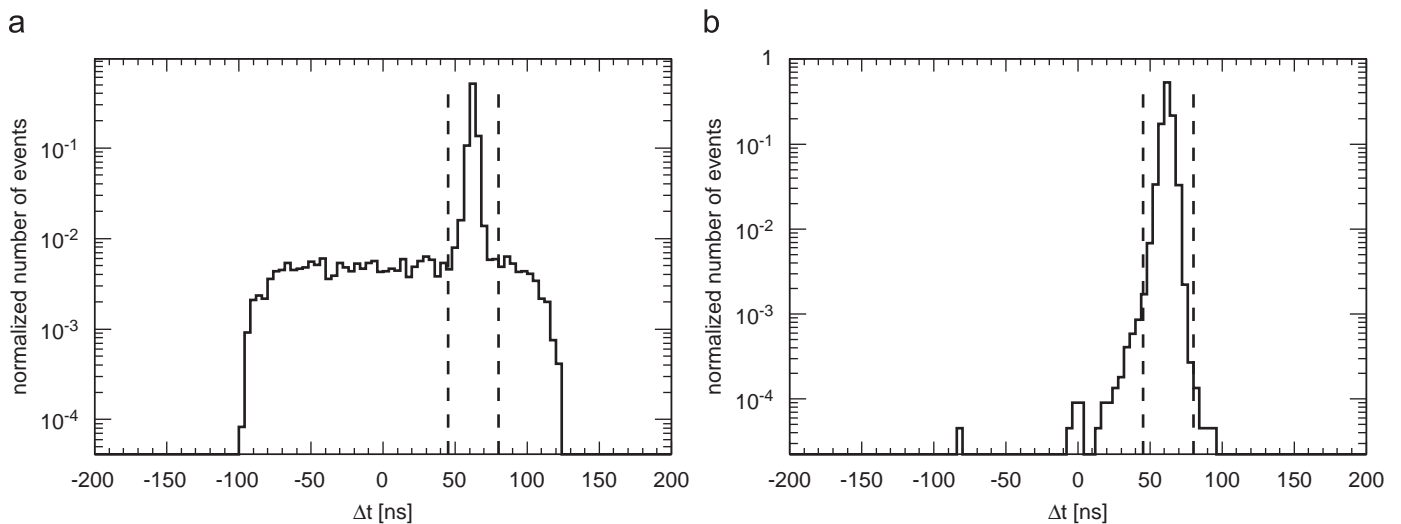


**Fig. 4.** Distributions of  $\Delta t = t_{pulse} - t_{trigger}$  for TileCal cells with a signal larger than 75 MeV (a) for a 9 GeV pion beam, (b) for a 100 GeV pion beam where no out-of-time particles are expected. The region selected in the analysis is shown.

has been used both to select single track events and for pion/electron separation.

The electromagnetic calorimetry consisted of one module of the Liquid Argon (LAr) calorimeter [10] built for the test. The module was placed inside a cryostat made of aluminum. Beam entrance and exit walls were each 0.1 interaction lengths thick. The calorimeter has four longitudinal layers, including a pre-sampler. The coverage of all four compartments is  $0 < \eta < 1.4$  and  $-\pi/16 < \phi < \pi/16$  rad (see Figs. 2 and 3 for  $\eta$  and  $\phi$  orientation convention). The  $\eta$ - $\phi$  granularity of each longitudinal sample is described in Ref. [10].

The hadronic calorimetry was composed of three modules of the scintillating tiles calorimeter (TileCal) [11]. The TileCal modules were placed about 30 cm behind the LAr calorimeter.<sup>3</sup> The total coverage of these three TileCal modules was  $-1 < \eta < 1$  and  $-3\pi/64 < \phi < 3\pi/64$  rad. Each TileCal module has three longitudinal layers, whose  $\eta$ - $\phi$  granularity is described in Ref. [11]. LAr and TileCal were both supported by a mobile table. This table was oriented in such a way that the incoming particles in the calorimeters were projective in pseudo-rapidity, as in the ATLAS experiment.

Various sections of the ATLAS muon spectrometer [12] were also present in the 2004 CTB setup. This sub-detector has not been used for the analysis presented in this paper.

### 3. Event selection

A critical issue in the very low-energy pion analysis is the purity of the pion sample. The pion selection cuts applied sequentially will be described in this section.

Only events in which a single particle reaches the calorimeters are selected (cut 1). This selection is obtained by requiring exactly one reconstructed TRT track with more than 30 LT hits (see Section 2).

To select particles with a well-defined trajectory through the beam line, a hit in at least one of the two planes of each BC is required (cut 2). In particular the presence of a hit in BC-2 ensures that one incident particle has passed through the VLE line. In this way we reduce the contamination from the high-energy halo muons passing through the beam dump (see Fig. 1).

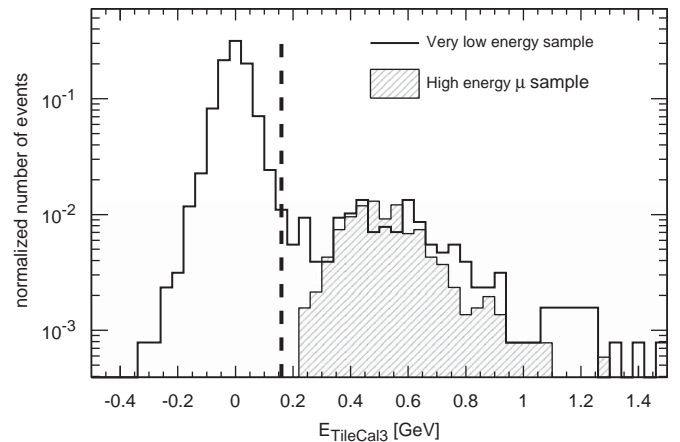


**Fig. 5.** Distribution of the energy deposited in the 3rd sample of TileCal,  $E_{TileCal3}$ . The empty distribution corresponds to a 7 GeV  $\eta_{beam} = 0.2$  pion beam with high-energy muon contamination. The hatched distribution corresponds to a 20 GeV muon beam at  $\eta_{beam} = 0$ . Events with  $E_{TileCal3} < 160$  MeV were selected in the analysis.

When a very low-energy particle triggers the data acquisition system, a high-energy muon from the halo may arrive close enough in time to be registered together with the low-energy particle. The signal produced in TileCal by halo muons is, in general, not synchronous with the trigger. This feature can be exploited to reject some of the high-energy halo muons. The time difference  $\Delta t$  between the time of the reconstructed signal shape in each cell of TileCal ( $t_{pulse}$ ) [13] and the trigger time ( $t_{trigger}$ ) was computed. Fig. 4(a) shows the distribution of  $\Delta t$  in a 9 GeV pion beam run. Only cells with a signal greater than 75 MeV<sup>4</sup> enter the distribution. The sharp peak at  $\Delta t \approx 50$  ns corresponds to particles in time with respect to the trigger while the large uniform tails are due to out-of-time particles. In Fig. 4(b) the distribution of  $\Delta t$  in TileCal cells for a 100 GeV pion beam is shown for comparison. A negligible number of out-of-time events are expected in this case. Only events with  $45 < \Delta t < 80$  ns in all TileCal cells with a signal larger than 75 MeV are kept (cut 3).

<sup>3</sup> In ATLAS this distance is 25 cm.

<sup>4</sup> 75 MeV corresponds to about three times the r.m.s of the cell electronic noise.

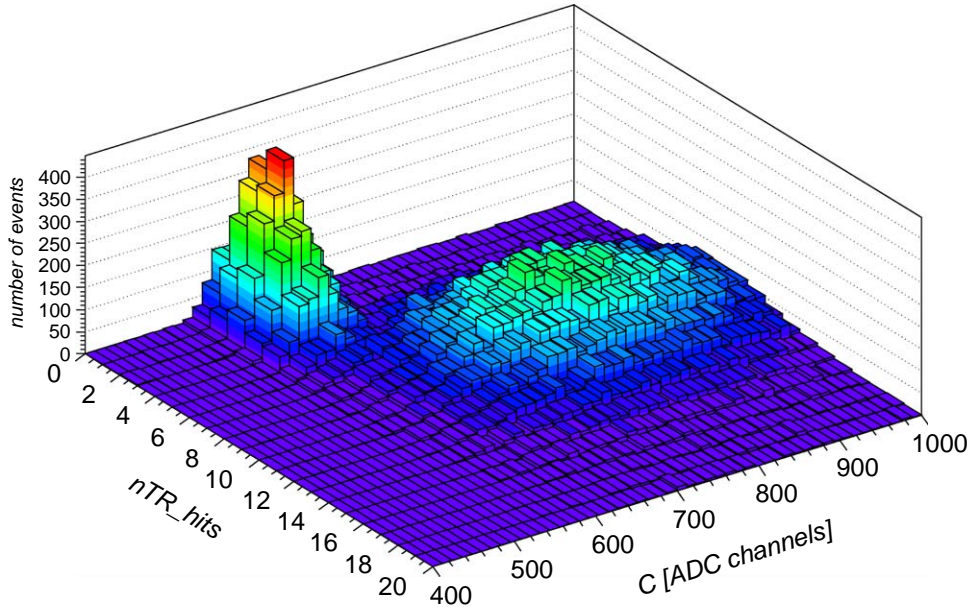


**Fig. 6.** Three-dimensional plot of the signal measured in the Cherenkov counter (C) and the number of hits per track produced by transition radiation reconstructed in the TRT ( $n_{TR\_hits}$ ). This distribution is for a 9 GeV beam.

**Table 1**

Event rejection chains for data collected using incident pions at  $\eta_{beam} = 0.35$  and nominal energies 3, 5, 7 and 9 GeV.

$E_{nom}$ (GeV)	3	5	7	9
Beam trigger events	93 961	94 771	94 158	94 446
Cut 1: only one track with more than 30 hits in TRT	61 608	61 833	61 073	63 053
Cut 2: a hit in at least one of the two projections of each BC	17 710	30 966	38 063	45 636
Cut 3: no out-of-time cells in TileCal	16 823	27 352	33 639	40 374
Cut 4: $E_{TileCal3} < 160\text{ MeV}$	16 214	26 109	32 441	39 123
Cut 5: $n_{TR\_hits} < 3$	955	1217	2230	3104
Cut 6: $C < 600$ ADC channels	141	395	1218	1803

Further reduction of the halo muon contamination was obtained by exploiting the fact that muons penetrate farther into material than pions. Low-energy pions are not expected to deposit a large fraction of their energy in the last longitudinal layer of TileCal (TileCal3). High-energy muons, on the other hand, will reach TileCal3 and produce a signal. Fig. 5 shows the energy released in TileCal3 for a pure 20 GeV muon sample and for a 7 GeV pion sample contaminated by halo muons. The peak around zero corresponds to the pedestal and is due to VLE pions that do not reach TileCal3. The peak around 500 MeV corresponds to the typical energy deposit from high-energy muons. Requiring a small energy deposition  $E_{TileCal3}$  in TileCal3<sup>5</sup> reduces the contamination from high-energy muons. The selection  $E_{TileCal3} < 160\text{ MeV}$  (vertical line in Fig. 5) has been applied to select low-energy pions (cut 4). This cut may introduce a small bias in the pion energy reconstruction because it rejects pions interacting late in the calorimeters. A Monte Carlo simulation shows that the fraction of pions which are rejected by cut 4 is less than 10%. This leads to a maximum decrease of 5% of the mean energy of the reconstructed pions. This cut was also applied to the simulated data.

Electrons were rejected making use of the signal (C) measured in the Cherenkov counter and the number of HT hits ( $n_{TR\_hits}$ ) produced in TRT. The Cherenkov pressure [6] was set such that the pions and muons at 9 GeV were below threshold and electrons

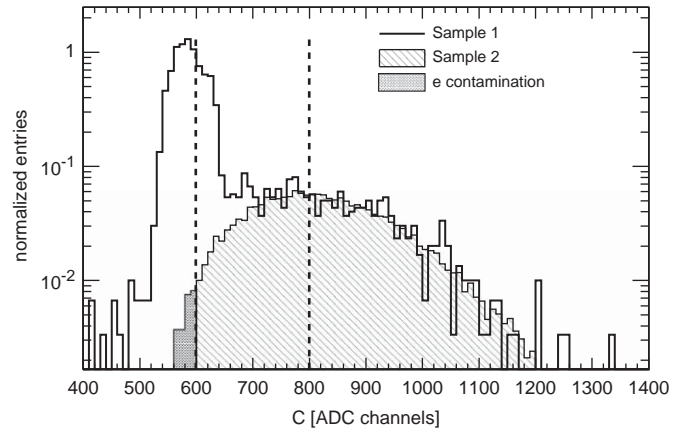


**Fig. 7.** Distributions of the Cherenkov signal C for Sample 1 (pions and electrons) and Sample 2 (only electrons) in the case of a 9 GeV beam. The Cherenkov cuts  $C = 600$  ADC (pion selection cut) and  $C = 800$  ADC (electron selection cut) are indicated by the dashed lines. The dark region corresponds to the extrapolated electron contamination in the pion sample.

above. Electrons are expected to produce an average of 6.1 TRT HT hits per track at 3 GeV and 6.5 hits at 9 GeV, while pions (and muons) will produce an average of 1.1 hits per track in the energy range 3–9 GeV [14]. Fig. 6 shows the three-dimensional distribution of the Cherenkov signal C versus  $n_{TR\_hits}$  in the case of a 9 GeV beam. Two regions can be identified, one

<sup>5</sup> The energy in TileCal3 is computed by summing the energy in the cells of the last TileCal sample in the pseudo-rapidity region  $\eta_{beam} - 0.3 < \eta_{cell} < \eta_{beam} + 0.3$ .

**Table 2**  
Estimated electron contamination  $f_e$  and decay muons contamination  $f_{decay \mu}$ .

$E_{nom}$ (GeV)	$\eta = 0.20$	$\eta = 0.25$	$\eta = 0.35$	$\eta = 0.45$	$\eta = 0.55$	$\eta = 0.65$
Electron contamination (%)						
3	$9 \pm 1$	$10 \pm 2$	$8 \pm 1$	$8 \pm 2$	$11 \pm 2$	$8 \pm 1$
4	$3.6 \pm 0.4$	–	$8 \pm 1$	$4.1 \pm 0.4$	$4.3 \pm 0.5$	$3.4 \pm 0.4$
5	$2.2 \pm 0.2$	–	$2.4 \pm 0.2$	$2.1 \pm 0.1$	$2.3 \pm 0.2$	–
6	$1.05 \pm 0.09$	$1.2 \pm 0.1$	$0.95 \pm 0.09$	$1.1 \pm 0.1$	$1.08 \pm 0.09$	$1.2 \pm 0.1$
7	$0.71 \pm 0.06$	–	$0.63 \pm 0.06$	$0.8 \pm 0.1$	$0.65 \pm 0.06$	$0.64 \pm 0.06$
8	$0.65 \pm 0.05$	$0.53 \pm 0.04$	$0.68 \pm 0.06$	$0.69 \pm 0.06$	$0.56 \pm 0.05$	–
9	–	$0.38 \pm 0.03$	$0.45 \pm 0.04$	$0.49 \pm 0.06$	$0.36 \pm 0.03$	$0.38 \pm 0.04$
Low-energy muons contamination (%)						
3	–	–	$1.8 \pm 0.5$	$2.1 \pm 0.6$	$3.0 \pm 0.8$	$3.4 \pm 0.9$

The decay muon contamination is negligible at energies higher than 3 GeV. At 3 GeV it is negligible for  $\eta_{beam} < 0.35$  (see the text).

populated by electrons (high  $C$  and  $nTR\_hits$  values) and the other by pions and muons (small  $C$  and  $nTR\_hits$  values). Electrons are rejected applying the cuts  $C < 600$  ADC channels (cut 5) and  $nTR\_hits < 3$  (cut 6).

The number of events passing the selection criteria are reported in Table 1 for pions at  $\eta_{beam} = 0.35$  and nominal energies  $E_{nom}$  of 3, 5, 7 and 9 GeV. All other runs show similar cut efficiencies, demonstrating a satisfactory stability of the beam conditions and of the detector operations during the data taking. The number of events in pion samples ( $N_\pi$ ) is about 100 at 3 GeV and increases up to about 2000 at 9 GeV.

## 4. Pion sample contamination

### 4.1. Electron contamination

The residual electron contamination in the pion sample was estimated. Two samples of particles were considered.

- Sample 1: cuts 1–5 are applied (cut 6 on the Cherenkov counter is not applied). This sample corresponds to pions with significant electron contamination.
- Sample 2: cuts 1–4 are applied together with the condition  $nTR\_hits \geq 8$ . This sample corresponds to a pure electron sample (pions do not give such a high number of HT hits per track).

Fig. 7 shows the distributions of the signal  $C$  in the Cherenkov counter for Samples 1 and 2 ( $E_{nom} = 9$  GeV). The two distributions are normalized in the region  $C > 800$  ADC where only electrons give a signal. The shapes are in good agreement in this region. The electron contamination corresponds to the normalized number of events of Sample 2 lying in the region  $C < 600$  ADC. The fractional contamination  $f_e$  can be obtained using the formula

$$f_e = \frac{N_{Sample1}[C > 800 \text{ ADC}]}{N_{Sample2}[C > 800 \text{ ADC}]} \times \frac{N_{Sample2}[C < 600 \text{ ADC}]}{N_{Sample1}[C < 600 \text{ ADC}]} \quad (1)$$

where  $N_{Sample1}$  and  $N_{Sample2}$  are the number of events for each sample in the region specified in the square brackets.

The values of  $f_e$  obtained for different nominal beam energies and pseudo-rapidities are reported in Table 2. The uncertainties in  $f_e$  are given by the quadratic sum of the statistical and the systematic errors. The systematic uncertainty was studied by varying the cuts used in Eq. (1) to normalize Samples 1 and 2 (from  $C = 700$  to 900 ADC), and varying the TRT cut used to select Sample 2 ( $nTR\_hits$  from 7 to 9). Systematic uncertainty is defined as half of the maximum difference between the values of  $f_e$ .

### 4.2. Decay muon contamination

A significant fraction of low-energy pions are expected to decay before reaching the calorimeters, producing low-energy muons. Two types of low-energy muons were distinguished:

1. Muons from pion decay in the tertiary beam prior to the momentum selection. These muons have an energy equal to the beam energy  $E_{beam}$ .
2. Muons from pion decay after the momentum selection. These muons are produced with an energy uniformly distributed between  $E_{max} = E_{beam}$  and  $E_{min} \approx 0.6 \times E_{beam}$ .<sup>6</sup>

The residual muon contamination in the pion sample was estimated by computing the fraction of muons (of types 1 and 2) that trigger the DAQ system and then computing how many of them pass all the analysis selection cuts.

The fraction of muons that trigger the DAQ was estimated in two different ways. First, it was determined in analysis of a previous test beam [15] at 3, 5 and 9 GeV (method 1). The beam geometry and composition were similar to the one discussed here, while the experimental layout was a rather simplified version of the one used for this analysis. Second, an independent computation using a beam transport program was used (method 2). The results of these two estimates are shown in Fig. 8. They show good agreement at 5 and 9 GeV but not at 3 GeV. At all beam energies the muon contamination was estimated to be the average of the two estimates and the uncertainty was taken to be half of the difference between the two estimates.

A Monte Carlo simulation was used to compute what fraction of muons passes all of the analysis cuts ( $f_{decay \mu}$ ). The fraction is negligible (lower than 1%) for all energies above 3 GeV. Table 2 shows the average fraction of contaminating muons. The quantity  $f_{decay \mu}$  increases with the pseudo-rapidity as the depth of the calorimeters increases and is negligible (lower than 1%) for  $\eta_{beam} < 0.35$ .

### 4.3. Halo muon contamination

Halo muons from the secondary beam line are not stopped by the beam dump (see Fig. 1) and have a wide energy spectrum (up to the secondary beam energy). In this analysis they are rejected by cuts 3 and 4 (see Table 1). The efficiency of these cuts has been measured using reference samples of 20 GeV muons.<sup>7</sup> As shown in

<sup>6</sup> The energy distribution of the muons reaching the calorimeters is not uniform and depends on the trigger acceptance (size of trigger scintillation counters).

<sup>7</sup> Data with 20 GeV muons were recorded during the high-energy data-taking of the 2004 CTB.

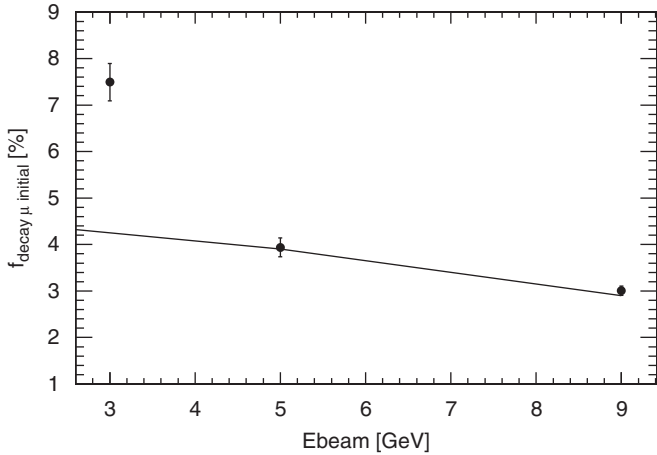


**Fig. 8.** Fraction of the decay muons in the pion sample at the front of the calorimeter as a function of the beam momentum. The fraction  $f_{\text{decay } \mu \text{ initial}}$  is defined as the number of muons triggering the DAQ divided by the number of pions. The full points show the result of the data-based analysis (method 1 in the text) and the solid curve represents the results obtained by the simulation (method 2 in the text).

**Fig. 5.** no high-energy muons are expected to deposit less than 160 MeV in the last TileCal layer (at  $\eta = 0$ ). The upper limit on the fraction of halo muons that enters the pion sample is 1% at 3 GeV and 0.2% at 9 GeV (at 95% confidence level). On the basis of this result, high-energy muon contamination in the pion samples has been neglected.

## 5. Reconstruction of the pion energy in the calorimeters

### 5.1. The energy scale in calorimeters

The cell energy  $E_{\text{cell}}$  in LAr was reconstructed by the optimal filtering coefficients method [16]. The LAr electromagnetic energy scale was determined comparing the measured and simulated energy response of 180 GeV electrons [17].

In TileCal, the fit filter method [13] was used to determine the cell energy. The electromagnetic scale of the reconstructed cell energy was obtained using electron beams incident at the center of each cell with an angle of  $20^\circ$  [13].

The shower energy in the calorimeter was obtained as

$$E_{\text{raw}} = E_{\text{raw}}(\text{LAr}) + E_{\text{raw}}(\text{TileCal}). \quad (2)$$

The quantities  $E_{\text{raw}}(\text{LAr})$  and  $E_{\text{raw}}(\text{TileCal})$  are, respectively, the sum of the energy deposited in the front, middle and back samples of LAr, and the sum of the energy deposited in the first and second samples of TileCal. Since the pions have not yet developed a shower, the signal in the LAr pre-sampler is dominated by noise and this layer was not considered in the calculation of  $E_{\text{raw}}$ . The energy measured in each of the two calorimeters is defined as the sum of the energy deposited in all calorimeters cells energy having a pseudo-rapidity coordinate  $\eta_{\text{beam}} - 0.15 \leq \eta_{\text{cell}} \leq \eta_{\text{beam}} + 0.15$ . No corrections for dead material, containment and non-compensation effects were applied. In order to improve the energy resolution, only cells with an energy  $E_{\text{cell}}$  larger than twice the standard deviation of the electronic noise  $\sigma_{\text{noise}}$  (in absolute value) were considered in the sum (2):

$$|E_{\text{cell}}| > 2 \times \sigma_{\text{noise}}. \quad (3)$$

### 5.2. The electronic noise

The standard deviation  $\sigma_{\text{noise}}$  of the electronic noise distribution varies from cell to cell, with large variations between

different longitudinal layers. For each run,  $\sigma_{\text{noise}}$  has been determined for each cell of the calorimeter using pedestal events, obtained from random triggers between beam bursts. Typical  $\sigma_{\text{noise}}$  values are 12 MeV (first layer of LAr), 28 MeV (second layer of LAr), 22 MeV (third layer of LAr), 30 MeV (first layer of TileCal), 30 MeV (second layer of TileCal) and 25 MeV (third layer of TileCal). The typical number of cells considered in the computation of the energy in the calorimeters is  $\approx 40$ . The total expected standard deviation of the electronic noise is  $\approx 160$  MeV. This value is negligible with respect to the energies reconstructed in the calorimeter (see Section 6.1) and has a negligible effect on the pion energy resolution.

### 5.3. Residual pedestal uncertainty

Given the small energy deposit and the large number of cells that are considered in the computation of  $E_{\text{raw}}$  (2), any deviation from zero of the pedestal signals has a significant effect on the total energy reconstructed in the calorimeters. For this reason, particular care was given to the study of pedestal levels of the calorimeters cells.

In the case of LAr, special runs were taken every 8 h during the data taking. For each cell and electronic gain setting, pedestals were recorded in each of the seven time windows in which the cell pulse is sampled. The mean pedestal in a cell was obtained as the average of the seven measurements. Corrections were also applied to take into account the drift due to changes of the temperature of the electronics front-end boards during the data-taking. The typical size of these corrections on the reconstructed energies was about 10 MeV [16].

In the case of TileCal the fit method applied to reconstruct the cell energy uses nine time samples with an event-by-event baseline subtraction and therefore corrects for any pedestal shifts.

The residual effect of a pedestal shift ( $E_{\text{res}}$ ) on the reconstructed energy was estimated for each run using the formula

$$\langle E_{\text{res}} \rangle = \langle E_{\text{ped}} \rangle \frac{\langle n_{\text{cell}} \rangle}{N_{\text{cell}}} \quad (4)$$

where  $\langle E_{\text{ped}} \rangle$  is the residual pedestal value in the reconstruction volume, and  $N_{\text{cell}}$  is the total number of the cells in this region. The quantity  $\langle n_{\text{cell}} \rangle$  is the average number of cells that satisfy the noise cut condition given by Eq. (3). The absolute value of the pedestal shift was found to be smaller than 2 MeV. This effect is negligible in comparison to the typical reconstructed pion energies (see Section 6.1).

### 5.4. Hot and dead LAr cell effects

Out of a total of about 2000 channels, 16 dead channels and four hot channels<sup>8</sup> were found in the LAr calorimeter. Dead and hot cells were not included in the computation of the total energy. Their signal was replaced by the average signal recorded in nearby cells in the  $\eta$ - $\phi$  plane.

The worst situation was in the first LAr layer, where 4 dead and 1 hot contiguous cells were found in the region  $\phi_{\text{cell}} = 0.049$  rad and  $\eta_{\text{cell}} \approx 0.65$ . The maximum estimated correction for these cells was found to be 36 MeV for the run with nominal beam energy 9 GeV and  $\eta_{\text{beam}} = 0.65$ . For almost all of the other data points the effects were smaller than 10 MeV. The uncertainties on the corrections applied to the reconstructed pion energies  $E_{\pi}$  are smaller than 10 MeV. This error is negligible compared to

<sup>8</sup> Hot cells were determined by studying the transversal shower profiles. They were identified as the ones with a signal larger than two times those of the neighboring cells.

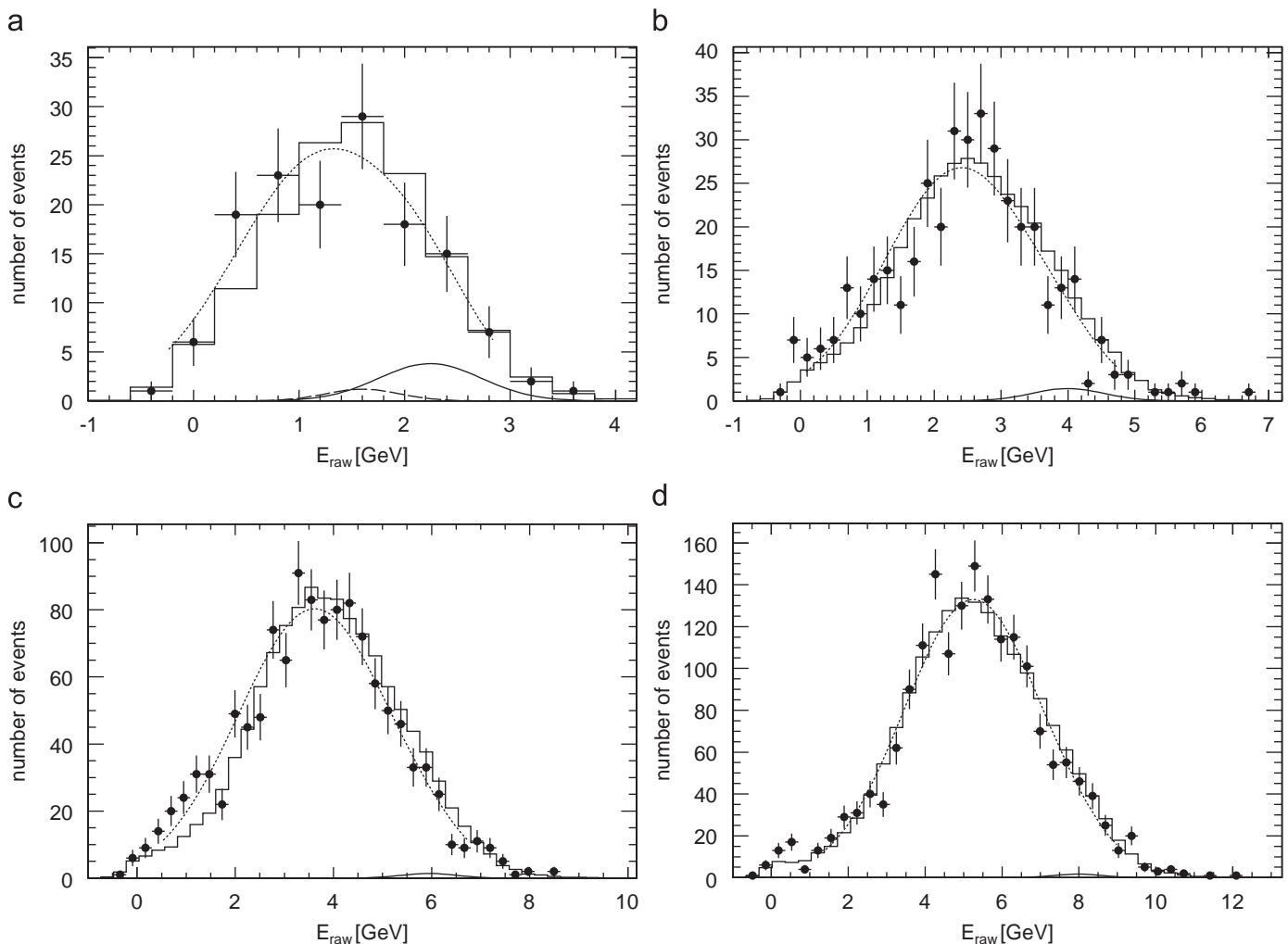


**Fig. 9.** Distribution of the reconstructed energy  $E_{raw}$  (see Eq. (2)) obtained for 3 GeV (a), 5 GeV (b), 7 GeV (c) and 9 GeV (d) at  $\eta_{beam} = 0.35$ . The full points represent the experimental data. The dashed curves correspond to the fit of Eq. (5) to the data. The solid curve represents the expected contribution of the electron contamination. At 3 GeV, the long-dashed curve shows the expected contribution from the decay muons. The histograms correspond to the prediction of the Monte Carlo simulation (see Section 7 for more details).

the statistical uncertainty on the reconstructed energies (see Section 6.1).

## 6. Calorimeter response to pions

### 6.1. Determination of the pion response

The pion response has been measured for pion samples at various energies and pseudo-rapidities. Fig. 9 shows the energy deposit  $E_{raw}$  distributions in the ATLAS calorimeter system when the pion beam impinged on the calorimeter at  $\eta = 0.35$  and for pion of nominal energies  $E_{nom} = 3, 5, 7$  and 9 GeV. The full points represent the experimental data.

The pion response  $E_{\pi}$  and the resolution  $\sigma_{\pi}$  of the calorimeter measurement are defined by the following function:

$$f(E_{raw}) = N \left[ \frac{(1 - f_e - f_{decay \mu})}{\sigma_{\pi} \sqrt{2\pi}} e^{-(E_{\pi} - E_{raw})^2 / 2\sigma_{\pi}^2} + \frac{f_e}{\sigma_e \sqrt{2\pi}} e^{-(E_e - E_{raw})^2 / 2\sigma_e^2} + \frac{f_{decay \mu}}{\sigma_{\mu} \sqrt{2\pi}} e^{-(E_{\mu} - E_{raw})^2 / 2\sigma_{\mu}^2} \right]. \quad (5)$$

Function (5) has three free parameters,  $E_{\pi}$ ,  $\sigma_{\pi}$  and the normalization factor  $N$ , determined by fitting to the data. The quantity  $f_e$  is the measured fraction of electrons in the pion samples (the

numerical values are reported in Table 2). The parameters  $E_e$  and  $\sigma_e$  are determined independently and they correspond to the mean and sigma values obtained by fitting a Gaussian to the distribution of  $E_{raw}$  (Eq. (2)) for pure electron samples. Such electron samples were obtained applying the selection cuts 1–4 (see Table 1) and requiring  $C > 800$  ADC channels and  $nTR\_hits > 8$ . Fig. 10(a) shows an example of the  $E_{raw}$  distribution obtained in the case of a 7 GeV electron sample at  $\eta_{beam} = 0.35$ . The Gaussian fit is performed in a region  $\pm 2\sigma$  around the mean value.

The estimated fraction  $f_{decay \mu}$  of low-energy muons in the pion sample (see Section 4.2) is significant only for the 3 GeV pion sample at  $\eta_{beam} \geq 0.35$ . The contribution of the low-energy muons is modeled as a Gaussian function with mean value  $E_{\mu}$  and width  $\sigma_{\mu}$ .  $E_{\mu}$  and  $\sigma_{\mu}$  are obtained from the simulated response to a sample of 1.8 GeV muons.<sup>9</sup> An example of the energy distribution for 1.8 GeV decay muons is given in Fig. 10(b). The Gaussian fit is performed in a region  $\pm 2\sigma$  around the mean value.

The pion sample distributions of  $E_{raw}$  are fitted by the function (5) in a region  $\pm 2\sigma$  around the mean value.<sup>10</sup> The Maximum

<sup>9</sup> 1.8 GeV is the most probable energy released by decay muons that do not reach the third sample of TileCal.

<sup>10</sup> An iterative procedure has been applied in order to get stable values of  $E_{\pi}$  and  $\sigma_{\pi}$ .

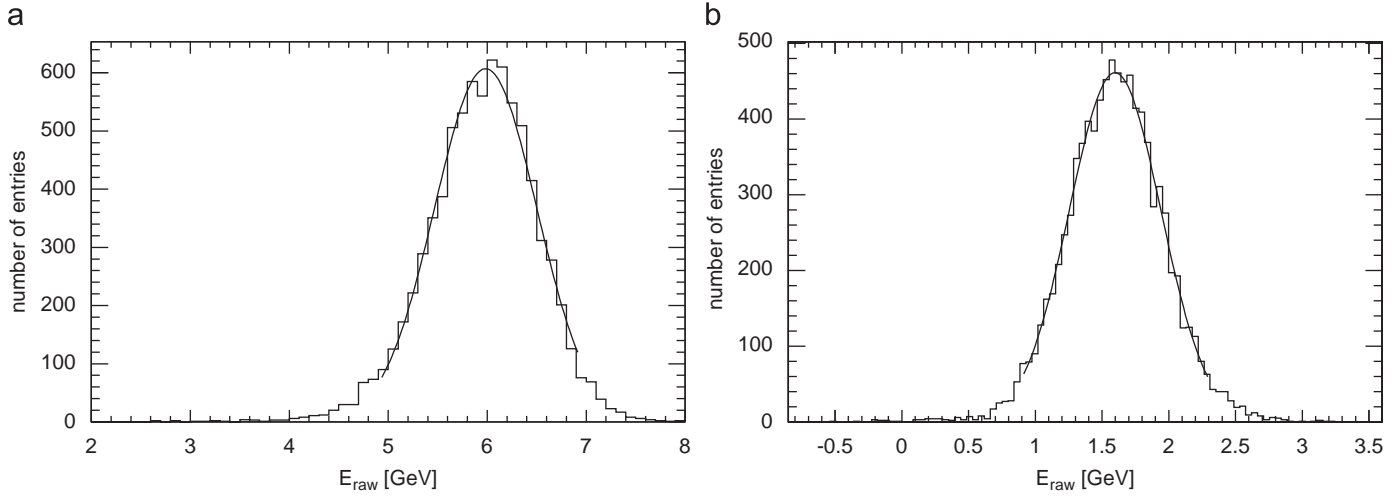


**Fig. 10.** (a)  $E_{\text{raw}}$  (Eq. (2)) distribution for a sample of 7 GeV electrons at  $\eta_{\text{beam}} = 0.35$ . The curve corresponds to a Gaussian fit performed to determine  $E_e$  and  $\sigma_e$ . (b) Monte Carlo distribution for a sample of 1.8 GeV muons produced in the decays of beam pions at  $\eta = 0.35$  (see the text).

Likelihood method was used in the fits because of the small statistics of the samples. The fit function (5) is superimposed on the data distributions of Fig. 9. The results of the fit procedure for  $E_\pi$  and  $\sigma_\pi$  are reported in Table 3.

Three sources of systematic uncertainty were considered:

1. uncertainty on the electron ( $f_e$ ) and decay muon ( $f_{\text{decay } \mu}$ ) contaminations,
2. uncertainty on the LAr and TileCal energy scales,
3. non-uniformity in  $\eta$  and  $\phi$  of the LAr and TileCal energy response.

The systematic error due to the uncertainty of the electron contamination  $f_e$  is estimated by replacing  $f_e$  with values  $\pm 1\sigma$  from the central value (see Table 2), and repeating the fit of Eq. (5) to the data.  $\Delta E_\pi$  and  $\Delta\sigma_\pi$  are defined as half of the maximum difference of the fit results. The systematic effect on the reconstructed pion energy  $E_\pi$  is about 1% at 3 GeV, 0.7% at 4 GeV, and smaller at larger energies. The systematic uncertainty on  $\sigma_\pi$  is 1% at 3 and 4 GeV, and smaller for energies larger than 4 GeV. The same procedure was applied to compute the systematic errors due to the uncertainty on the decay muon contamination ( $f_{\text{decay } \mu}$ ). The relative systematic errors on  $E_\pi$  and  $\sigma_\pi$  are 0.3% and 0.5%, respectively.

The uncertainty on the LAr energy scale, due mainly to uncertainty in the knowledge of the beam momentum, is 0.7% [17]. The estimated error on the TileCal energy scale is 0.5% [13].

The systematic error due to the non-uniformity of the LAr and TileCal response was studied using electrons and pions beams. The numerical values obtained are 0.4% in the case of LAr [16] and 2% in the case of TileCal [13].

The errors on  $E_\pi$  and  $\sigma_\pi$  are reported in Table 3. The first error on  $E_\pi$  corresponds to the statistical uncertainty combined in quadrature with the systematic errors (1). The second error is due to the uncertainty of the energy scales (2). In this case the error values of the different data points are correlated. The LAr contribution dominates: it is equal to 7 MeV at 3 GeV and increases up to 25 MeV at 9 GeV. The third error comes from the uncertainty on the calorimeter uniformity response. The TileCal contribution dominates: it is equal to 7 MeV at 3 GeV and increases up to 45 MeV at 9 GeV. In the case of  $\sigma_\pi$  only the statistical uncertainty, which is much larger than all of the systematic effects, has been reported.

**Table 3**

Measured energy response  $E_\pi$  and the resolution  $\sigma_\pi$  obtained fitting Eq. (5) to data (see text).

$E_{\text{nom}}$ (GeV)	$\eta_{\text{beam}}$	$E_\pi$ (GeV)	$\Delta E_\pi$ (1) (GeV)	$\Delta E_\pi$ (2) (GeV)	$\Delta E_\pi$ (3) (GeV)	$\sigma_\pi$ (GeV)
3	0.20	1.38	0.07	0.008	0.007	$0.65 \pm 0.07$
3	0.25	1.2	0.1	0.007	0.007	$0.8 \pm 0.1$
3	0.35	1.25	0.09	0.007	0.007	$0.83 \pm 0.09$
3	0.45	1.3	0.1	0.007	0.006	$0.8 \pm 0.1$
3	0.55	1.0	0.1	0.006	0.005	$0.8 \pm 0.1$
3	0.65	1.11	0.08	0.006	0.005	$0.63 \pm 0.07$
4	0.20	1.83	0.09	0.009	0.01	$1.10 \pm 0.09$
4	0.35	1.7	0.1	0.010	0.009	$0.8 \pm 0.1$
4	0.45	1.78	0.08	0.009	0.01	$1.05 \pm 0.08$
4	0.55	1.84	0.09	0.009	0.01	$1.2 \pm 0.1$
4	0.65	1.70	0.07	0.010	0.008	$1.03 \pm 0.08$
5	0.20	2.34	0.06	0.01	0.02	$1.09 \pm 0.06$
5	0.35	2.42	0.07	0.01	0.02	$1.12 \pm 0.06$
5	0.45	2.45	0.05	0.01	0.02	$1.14 \pm 0.04$
5	0.55	2.28	0.07	0.01	0.01	$1.16 \pm 0.07$
6	0.20	3.02	0.06	0.01	0.02	$1.34 \pm 0.06$
6	0.25	3.15	0.06	0.02	0.02	$1.35 \pm 0.06$
6	0.35	2.96	0.05	0.02	0.02	$1.27 \pm 0.05$
6	0.45	2.95	0.05	0.02	0.02	$1.28 \pm 0.05$
6	0.55	2.96	0.06	0.02	0.02	$1.45 \pm 0.06$
6	0.65	2.83	0.05	0.02	0.02	$1.28 \pm 0.05$
7	0.20	3.78	0.05	0.02	0.03	$1.54 \pm 0.05$
7	0.35	3.64	0.05	0.02	0.03	$1.56 \pm 0.05$
7	0.45	3.62	0.07	0.02	0.03	$1.46 \pm 0.07$
7	0.55	3.67	0.05	0.02	0.03	$1.41 \pm 0.04$
7	0.65	3.59	0.05	0.02	0.02	$1.50 \pm 0.05$
8	0.20	4.26	0.05	0.02	0.03	$1.68 \pm 0.05$
8	0.25	4.49	0.05	0.02	0.04	$1.67 \pm 0.05$
8	0.35	4.40	0.05	0.02	0.03	$1.68 \pm 0.05$
8	0.45	4.43	0.05	0.02	0.03	$1.57 \pm 0.04$
8	0.55	4.36	0.05	0.02	0.03	$1.71 \pm 0.05$
9	0.25	5.30	0.06	0.02	0.05	$1.91 \pm 0.06$
9	0.35	5.26	0.05	0.02	0.04	$1.79 \pm 0.04$
9	0.45	5.23	0.07	0.03	0.04	$1.88 \pm 0.07$
9	0.55	5.06	0.05	0.03	0.04	$1.88 \pm 0.05$
9	0.65	4.91	0.07	0.03	0.03	$2.00 \pm 0.06$

The first error on  $E_\pi$  corresponds to the quadratic combination of the statistical error and the error due to the uncertainty on the contamination of electrons and muons (1). The second error on  $E_\pi$  is the systematic uncertainty on the energy scale (2) definition in LAr and TileCal (see text) and the third one corresponds to the non-uniformity of the energy scale in  $\eta$  and  $\phi$ . The errors on  $\sigma_\pi$  are dominated by the statistical ones.

## 6.2. Determination of the beam energies

The measurement of the energy response ratio  $R_{E_\pi} = E_\pi/E_{beam}$  requires knowledge of the beam energy. The VLE beam momentum can be computed using the formula [5]:

$$p^{VLE}[\text{GeV}] = \frac{299.79}{\theta[\text{mrad}]} \int B dl[\text{Tm}] \quad (6)$$

where the quantity  $\int B dl$  is the measured magnetic field integral of the bending magnet B4 and  $\theta$  is the beam deflection angle (see

**Table 4**  
Measured values of the beam energies.

$E_{nom}$ (GeV)	$E_{beam}$ (GeV)
3	$3.09 \pm 0.02 \pm 0.03$
4	$4.06 \pm 0.01 \pm 0.03$
5	$5.03 \pm 0.02 \pm 0.04$
6	$6.07 \pm 0.02 \pm 0.05$
7	$6.95 \pm 0.01 \pm 0.06$
8	$8.20 \pm 0.01 \pm 0.07$
9	$9.27 \pm 0.01 \pm 0.08$

The first error is due to the statistical uncertainty of the determination of  $p^{VLE}$ . The second error is the systematic uncertainty on  $S$  (see the text).

**Table 5**  
Energy response ratio measurements for pions of different energy and  $\eta_{beam}$ .

$E_{nom}$ (GeV)	$\eta_{beam}$	$R_{E_\pi}$	$\Delta R_{E_\pi}$ (1)	$\Delta R_{E_\pi}$ (2)	$\Delta R_{E_\pi}$ (3)	$(R_{E_\pi})_{MC}$
3	0.20	0.45	0.02	0.002	0.002	$0.432 \pm 0.001$
3	0.25	0.40	0.03	0.002	0.002	$0.456 \pm 0.001$
3	0.35	0.41	0.03	0.002	0.002	$0.447 \pm 0.001$
3	0.45	0.42	0.04	0.002	0.002	$0.454 \pm 0.001$
3	0.55	0.33	0.04	0.002	0.002	$0.445 \pm 0.001$
3	0.65	0.36	0.02	0.002	0.002	$0.443 \pm 0.001$
4	0.20	0.45	0.02	0.003	0.003	$0.466 \pm 0.001$
4	0.35	0.43	0.03	0.002	0.002	$0.491 \pm 0.001$
4	0.45	0.44	0.02	0.002	0.003	$0.489 \pm 0.001$
4	0.55	0.45	0.02	0.003	0.003	$0.479 \pm 0.002$
4	0.65	0.42	0.02	0.002	0.002	$0.474 \pm 0.001$
5	0.20	0.47	0.01	0.003	0.003	$0.494 \pm 0.001$
5	0.35	0.48	0.01	0.003	0.003	$0.517 \pm 0.001$
5	0.45	0.487	0.009	0.003	0.003	$0.516 \pm 0.001$
5	0.55	0.45	0.01	0.003	0.003	$0.510 \pm 0.001$
6	0.20	0.498	0.009	0.003	0.004	$0.512 \pm 0.001$
6	0.25	0.52	0.01	0.003	0.004	$0.542 \pm 0.001$
6	0.35	0.487	0.008	0.003	0.003	$0.540 \pm 0.001$
6	0.45	0.485	0.008	0.003	0.003	$0.540 \pm 0.001$
6	0.55	0.49	0.01	0.003	0.003	$0.533 \pm 0.001$
6	0.65	0.465	0.009	0.003	0.003	$0.529 \pm 0.001$
7	0.20	0.543	0.008	0.003	0.005	$0.526 \pm 0.001$
7	0.35	0.523	0.008	0.003	0.004	$0.557 \pm 0.001$
7	0.45	0.52	0.01	0.003	0.003	$0.557 \pm 0.001$
7	0.55	0.527	0.007	0.003	0.004	$0.549 \pm 0.001$
7	0.65	0.517	0.007	0.003	0.003	$0.544 \pm 0.001$
8	0.20	0.520	0.007	0.003	0.004	$0.542 \pm 0.001$
8	0.25	0.548	0.006	0.003	0.005	$0.578 \pm 0.001$
8	0.35	0.537	0.007	0.003	0.004	$0.573 \pm 0.001$
8	0.45	0.541	0.006	0.003	0.004	$0.573 \pm 0.001$
8	0.55	0.532	0.007	0.003	0.004	$0.563 \pm 0.001$
9	0.25	0.572	0.006	0.004	0.005	$0.586 \pm 0.001$
9	0.35	0.568	0.005	0.003	0.005	$0.583 \pm 0.001$
9	0.45	0.564	0.008	0.003	0.004	$0.581 \pm 0.001$
9	0.55	0.546	0.006	0.003	0.004	$0.574 \pm 0.001$
9	0.65	0.529	0.007	0.003	0.003	$0.570 \pm 0.001$

See Section 6.3 for details about the error determination. In the table the results obtained using a Monte Carlo (MC) simulation are also reported (see Section 7).

Fig. 1). The angle  $\theta$  is the average deflection angle computed for each event using the coordinate measurements of the beam impact point in the beam chambers BC-2, BC-1 and BC0 [5].

Systematic uncertainties on  $p^{VLE}$  are due to incomplete knowledge of the beam line geometry and the magnetic field integral. The response of the LAr calorimeter to electrons at each beam energy has been used to compute a correction factor  $S$ . The beam energy becomes

$$E_{beam} = S \times p^{VLE}. \quad (7)$$

In Eq. (7) the pion mass was neglected. The correction factor  $S$  was found to be  $0.972 \pm 0.008$  for all of the nominal beam energies. The determination of  $S$  is strongly correlated to the LAr energy scale discussed in Section 5.1. Details can be found in Ref. [17]. Table 4 shows the measured values of  $E_{beam}$ . The errors are due to the statistical uncertainty on  $p^{VLE}$  and the systematic uncertainty on  $S$ . The intrinsic beam energy dispersion is equal to 3.5% [17] and is negligible with respect to the resolution of the calorimetric measurements.

## 6.3. Measurements of the energy response ratio and of the fractional resolution

The measurement of the energy response ratio  $R_{E_\pi}$ , and of the fractional resolutions  $R_{\sigma_\pi} = \sigma_\pi/E_\pi$  are reported in Tables 5 and 6,

**Table 6**  
Fractional energy resolution measurements for pions of different energy and  $\eta_{beam}$ .

$E_{nom}$ (GeV)	$\eta_{beam}$	$R_{\sigma_\pi}$	$(R_{\sigma_\pi})_{MC}$
3	0.20	$0.470 \pm 0.060$	$0.565 \pm 0.003$
3	0.25	$0.600 \pm 0.100$	$0.547 \pm 0.003$
3	0.35	$0.660 \pm 0.090$	$0.567 \pm 0.003$
3	0.45	$0.600 \pm 0.100$	$0.561 \pm 0.003$
3	0.55	$0.800 \pm 0.100$	$0.572 \pm 0.003$
3	0.65	$0.560 \pm 0.070$	$0.587 \pm 0.003$
4	0.20	$0.600 \pm 0.060$	$0.515 \pm 0.003$
4	0.35	$0.480 \pm 0.090$	$0.483 \pm 0.002$
4	0.45	$0.590 \pm 0.050$	$0.493 \pm 0.002$
4	0.55	$0.610 \pm 0.060$	$0.508 \pm 0.004$
4	0.65	$0.610 \pm 0.050$	$0.516 \pm 0.003$
5	0.20	$0.460 \pm 0.030$	$0.461 \pm 0.002$
5	0.35	$0.460 \pm 0.030$	$0.432 \pm 0.002$
5	0.45	$0.470 \pm 0.020$	$0.435 \pm 0.002$
5	0.55	$0.510 \pm 0.030$	$0.442 \pm 0.002$
6	0.20	$0.440 \pm 0.020$	$0.437 \pm 0.002$
6	0.25	$0.430 \pm 0.020$	$0.398 \pm 0.002$
6	0.35	$0.430 \pm 0.020$	$0.396 \pm 0.002$
6	0.45	$0.430 \pm 0.020$	$0.400 \pm 0.002$
6	0.55	$0.490 \pm 0.020$	$0.409 \pm 0.002$
6	0.65	$0.450 \pm 0.020$	$0.415 \pm 0.002$
7	0.20	$0.410 \pm 0.010$	$0.414 \pm 0.002$
7	0.35	$0.430 \pm 0.020$	$0.381 \pm 0.002$
7	0.45	$0.400 \pm 0.020$	$0.383 \pm 0.002$
7	0.55	$0.380 \pm 0.010$	$0.389 \pm 0.002$
7	0.65	$0.420 \pm 0.010$	$0.399 \pm 0.002$
8	0.20	$0.390 \pm 0.010$	$0.396 \pm 0.002$
8	0.25	$0.370 \pm 0.010$	$0.351 \pm 0.002$
8	0.35	$0.380 \pm 0.010$	$0.359 \pm 0.002$
8	0.45	$0.350 \pm 0.010$	$0.362 \pm 0.002$
8	0.55	$0.390 \pm 0.010$	$0.369 \pm 0.002$
9	0.25	$0.360 \pm 0.010$	$0.338 \pm 0.002$
9	0.35	$0.342 \pm 0.009$	$0.345 \pm 0.002$
9	0.45	$0.360 \pm 0.010$	$0.346 \pm 0.001$
9	0.55	$0.370 \pm 0.010$	$0.351 \pm 0.002$
9	0.65	$0.410 \pm 0.010$	$0.357 \pm 0.001$

The errors are dominated by the statistical ones. The results obtained using a Monte Carlo (MC) simulation are also reported (see Section 7).

respectively. The values of  $R_{E_\pi}$  are  $\approx 40\%$  at 3 GeV and  $\approx 55\%$  at 9 GeV. The first error in the energy response ratio,  $\Delta R_{E_\pi}$  (1), is equal to the quadratic sum of the error on  $E_\pi$  (see Table 3) discussed in Section 6.1 and the error on  $p^{VE}$  (first error in Table 4). It varies between  $\approx 8\%$  at 3 GeV and  $\approx 1\%$  at 9 GeV. The second error,  $\Delta R_{E_\pi}$  (2), affects in the same way all the measurements of  $E_\pi/E_{beam}$ . It was obtained combining the uncertainties due to the calorimeter scale factors and  $S$ . The beam energy correction factor terms dominates. The third error,  $\Delta R_{E_\pi}$  (3), is due to the non-homogeneity of the calorimeters response. Below 6 GeV the LAR and TileCal contributions are comparable. Above 6 GeV, TileCal contribution dominates.

The values of  $R_{\sigma_\pi}$  are  $\approx 60\%$  at 3 GeV and  $\approx 40\%$  at 9 GeV. The contribution of the electronic noise to the resolution is  $\approx 15\%$  at 3 GeV and decreases to  $\approx 5\%$  at 9 GeV (see Section 5.2). Since it is added in quadrature to the other sources its contribution to the resolution is negligible. The largest uncertainty in the resolution is the statistical error.

The quantities  $R_{E_\pi}$  are shown in Fig. 11 (open circles) as a function of  $\eta_{beam}$  for different beam energies. They are also shown in Fig. 12 as a function of  $E_{beam}$  for different  $\eta_{beam}$  values. In the two figures the errors include statistical and systematic effects combined in quadrature. Fig. 13 shows the fractional resolutions  $R_{\sigma_\pi}$  as a function of  $1/\sqrt{E_{beam}}$  (open circles) for different  $\eta_{beam}$  values.

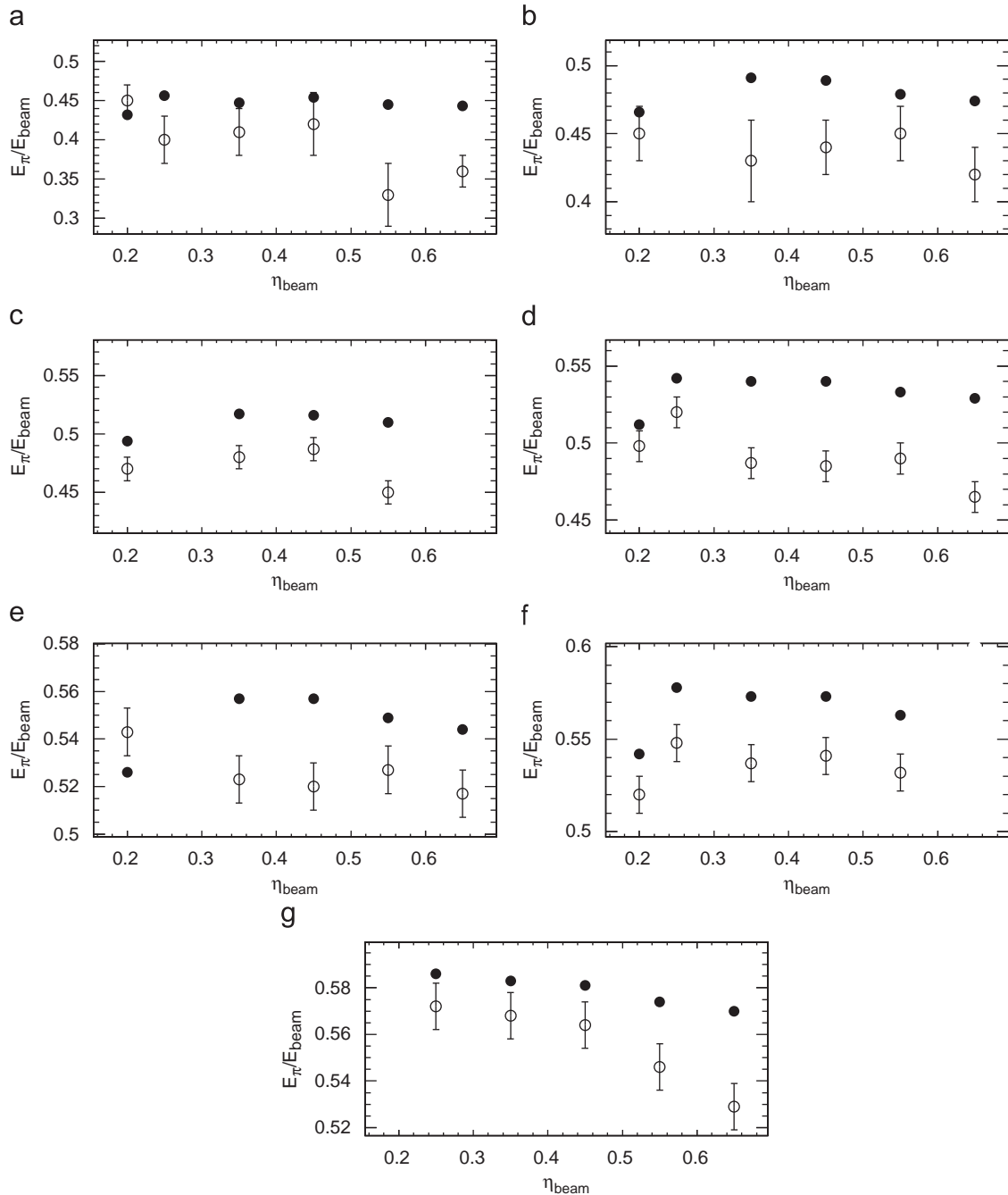


**Fig. 11.** Energy response ratios measured (open points) and predicted by Monte Carlo simulation (full points) as a function of  $\eta_{beam}$  for different beam energy values: (a) 3 GeV, (b) 4 GeV, (c) 5 GeV, (d) 6 GeV, (e) 7 GeV, (f) 8 GeV and (g) 9 GeV. The error includes statistical and systematic effects combined in quadrature.

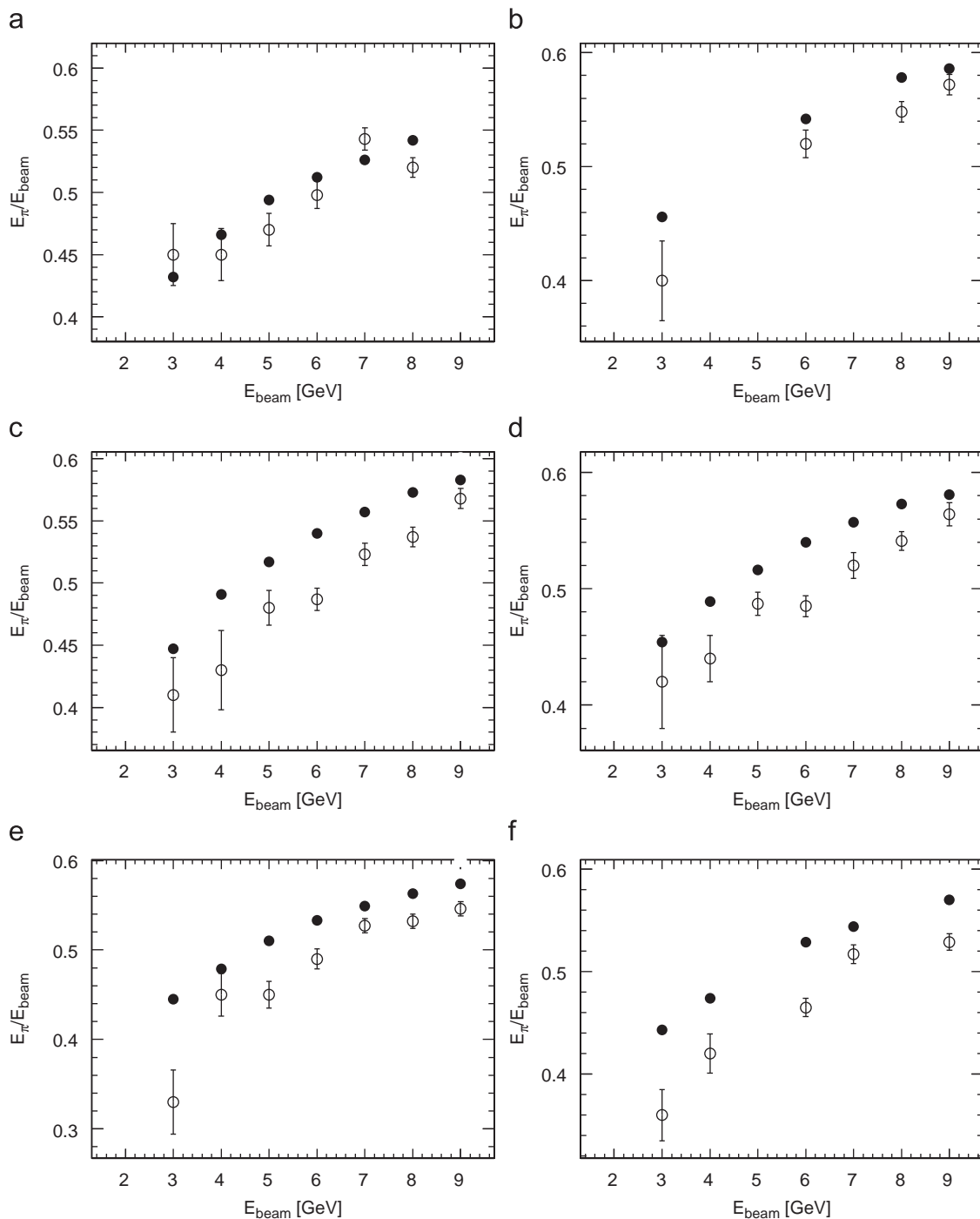


**Fig. 12.** Energy response ratio measured (open points) and predicted by Monte Carlo simulation (full points) as a function of  $E_{\text{beam}}$  for different  $\eta_{\text{beam}}$  values: (a) 0.20, (b) 0.25, (c) 0.35, (d) 0.45, (e) 0.55, and (f) 0.65. The error includes statistical and systematic effects combined in quadrature.

## 7. Comparison with Monte Carlo simulation results

The experimental results were compared to the predictions of the Monte Carlo simulation program Geant 4<sup>11</sup> [3] at the electromagnetic energy scale. For the MC the LAr and TileCal scales were obtained using the results from electron simulations (see Section 5.4). The QGSP-Bertini hadronic showering model was used in the simulation. This is the model presently being used

in the simulation of the response of the ATLAS detector to p-p events at 14 TeV.

In the simulation the detector material and geometry were fully described [3,4]. The mean and spread of the incoming pion beam momentum correspond to what was measured (see Section 6.2). The spatial and angular distributions of the beam were also tuned to reproduce the experimental ones.<sup>12</sup> The

<sup>11</sup> The version 9.1 has been used.

<sup>12</sup> The spatial distribution of the beam was measured using the beam chambers BC1 and BC2 (see Fig. 1).

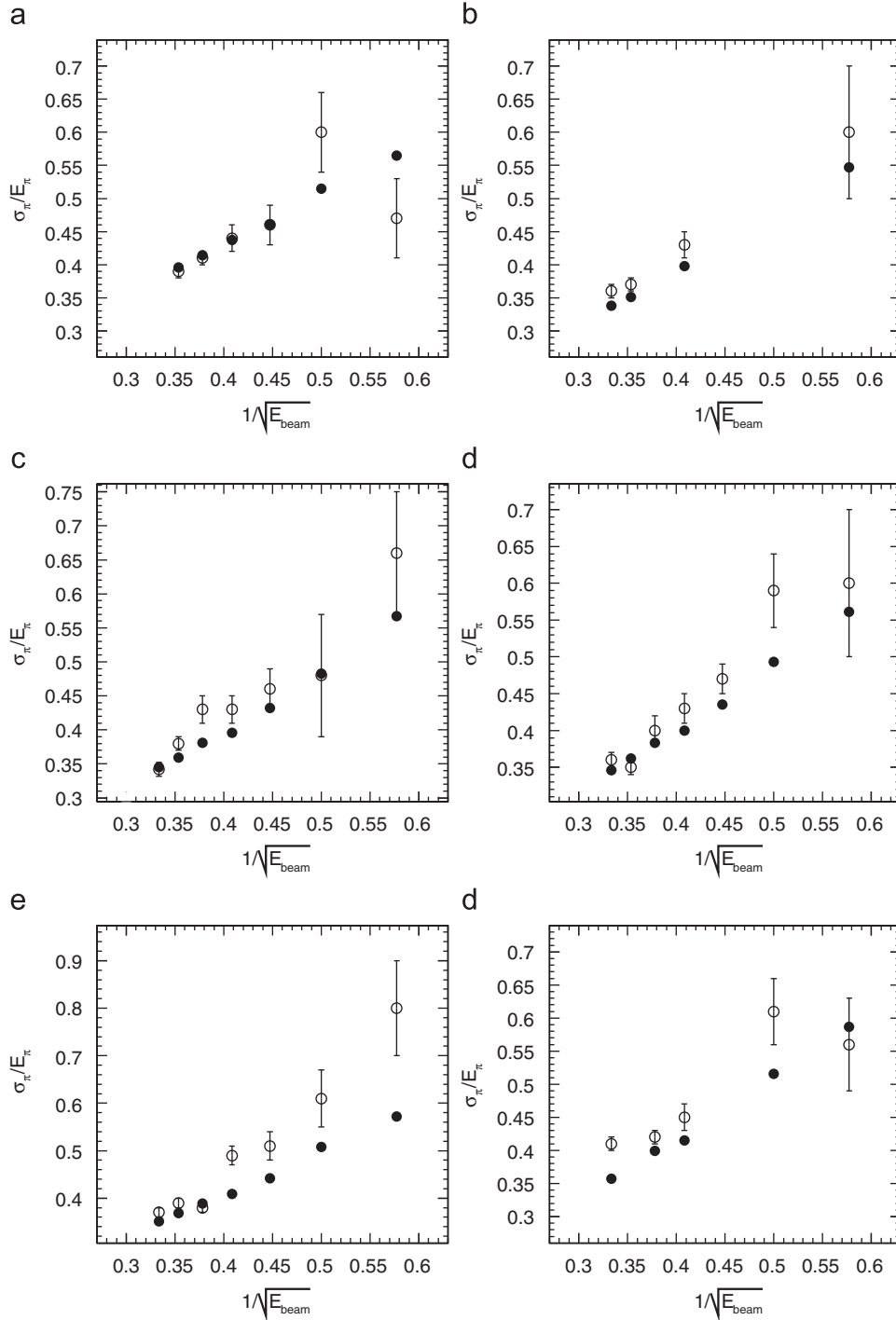


**Fig. 13.** Fractional resolutions measured (open circles) and predicted by the Monte Carlo simulation (full points) as a function of  $1/\sqrt{E_{beam}}$  for different values of  $\eta_{beam}$ : (a) 0.20, (b) 0.25, (c) 0.35, (d) 0.45, (e) 0.55, and (f) 0.65. The values of  $E_{beam}$  in the square roots are in GeV. The errors include statistical and systematic effects combined in quadrature.

measured electronic noise in the different calorimeter cells and the effects of photo statistics (70 phe/GeV) are included in the Monte Carlo simulation. A total of  $10^5$  events were simulated for each experimental point.<sup>13</sup>

<sup>13</sup> To reproduce the experimental situation, contamination from electrons and decay muons (in the case of the 3 GeV beam) has been added to the simulated pion sample. This contamination corresponds to what is reported in Table 2.

The distribution of the variable  $E_{raw}$  obtained with simulated data is shown in Fig. 9 for beam energies 3, 5, 7 and 9 GeV, and  $\eta_{beam} = 0.35$ . The distributions obtained with the Monte Carlo simulation were fit with Eq. (5) to determine  $E_\pi$  and  $\sigma_\pi$ . Results are reported in Tables 5 and 6. Figs. 11–13 show the Monte Carlo results (full points) together with data (open points).

The mean energy response of the simulated data is higher than that obtained with the experimental data and the distributions are narrower. The comparison between the data and the

**Table 7**

Relative difference of response (top) and resolution (bottom) between data and simulated events, for different values of the beam energy and pseudo-rapidity.

$E_{nom}$ (GeV)	$\eta = 0.20$	$\eta = 0.25$	$\eta = 0.35$	$\eta = 0.45$	$\eta = 0.55$	$\eta = 0.65$
$(R_{E_\pi})_{MC}/R_{E_\pi} - 1$ (%)						
3	$-4 \pm 5$	$14 \pm 10$	$10 \pm 8$	$9 \pm 10$	$36 \pm 15$	$23 \pm 8$
4	$4 \pm 5$	–	$15 \pm 9$	$11 \pm 5$	$6 \pm 5$	$14 \pm 5$
5	$6 \pm 3$	–	$8 \pm 3$	$6 \pm 2$	$13 \pm 4$	–
6	$3 \pm 2$	$4 \pm 2$	$11 \pm 2$	$11 \pm 2$	$9 \pm 2$	$14 \pm 2$
7	$-3 \pm 2$	–	$7 \pm 2$	$7 \pm 2$	$4 \pm 2$	$5 \pm 2$
8	$4 \pm 2$	$5 \pm 2$	$7 \pm 2$	$6 \pm 2$	$6 \pm 2$	–
9	–	$2 \pm 2$	$3 \pm 1$	$3 \pm 2$	$5 \pm 1$	$8 \pm 2$
$(R_{\sigma_\pi})_{MC}/R_{\sigma_\pi} - 1$ (%)						
3	$20 \pm 14$	$-13 \pm 14$	$-14 \pm 11$	$-6 \pm 17$	$-26 \pm 14$	$5 \pm 14$
4	$-15 \pm 8$	–	$0 \pm 18$	$-16 \pm 7$	$-17 \pm 8$	$-16 \pm 7$
5	$-1 \pm 6$	–	$-6 \pm 6$	$-7 \pm 4$	$-13 \pm 6$	–
6	$-2 \pm 4$	$-7 \pm 5$	$-8 \pm 4$	$-8 \pm 4$	$-16 \pm 4$	$-8 \pm 4$
7	$1 \pm 4$	–	$-12 \pm 3$	$-5 \pm 5$	$1 \pm 3$	$-5 \pm 4$
8	$1 \pm 3$	$-6 \pm 3$	$-6 \pm 3$	$2 \pm 3$	$-6 \pm 3$	–
9	–	$-6 \pm 3$	$1 \pm 3$	$-4 \pm 4$	$-5 \pm 3$	$-13 \pm 3$

The errors were obtained combining in quadrature the statistical and the systematic uncertainties as discussed in the text.

simulation can be quantified using the quantities

$$(R_{E_\pi})_{MC}/R_{E_\pi} - 1 \quad (8)$$

$$(R_{\sigma_\pi})_{MC}/R_{\sigma_\pi} - 1 \quad (9)$$

The results are reported in Table 7. Statistical and systematic uncertainties were combined in quadrature.

## 8. Conclusions

The characterization of the response of the ATLAS calorimeters to low-energy particles (below 10 GeV) is an important issue because low-energy particles carry a large fraction of the total energy of jets. Many strategies for establishing the jet energy scale in ATLAS rely on the Monte Carlo simulation of the calorimeters. Test beam data are very important to constrain, test and validate the simulation models.

A large amount of low-energy data was taken during the 2004 combined test beam. Pion and electron samples with energies between 3 and 9 GeV and an incident angle corresponding to pseudo-rapidities between 0.2 and 0.65 were recorded.

In this paper, a detailed analysis of the response in the electromagnetic and hadronic central calorimeters to low-energy pions is presented. Clean pion samples have been obtained after removing various sources of contamination (electrons and muons). The calorimeter response (reconstructed energy and energy resolution) was computed, taking into account the remaining contamination. All energies were reconstructed at the electromagnetic scale and without any correction for dead material and non-compensation of the calorimeters. Considering the statistical uncertainties and some sources of systematic errors (miscalibration of the beam energy, uncertainty on the contaminations), the ratio between the reconstructed pion energy and the beam energy has been determined with a precision varying from

$\approx 1\%$  at 9 GeV to  $\approx 8\%$  at 3 GeV. The error on the fractional resolution varies from  $\approx 14\%$  at 3 GeV to  $\approx 3\%$  at 9 GeV.

The measurements were compared to simulated results obtained using Geant 4. The simulation predicts a larger response and a lower energy resolution than what was measured. The relative difference response ratio between data and simulation depends on the beam energy and on  $\eta_{beam}$ , and ranges from  $\approx +5\%$  at 9 GeV to  $\approx +15\%$  at 3 GeV. The relative difference in fractional resolution depends also on  $\eta_{beam}$  and  $E_{beam}$ , and ranges from  $\approx -5\%$  at 9 GeV to  $\approx -15\%$  at 3 GeV. The agreement seems to improve at higher  $E_{beam}$  and to get worse at larger  $\eta_{beam}$ .

## Acknowledgments

A very important ingredient of the 2004 ATLAS CTB has been the mechanics of the two calorimeters support and movement. We would like to acknowledge Danilo Giugni, Simone Coelli and Giampiero Braga from INFN Milano for the design, overview of the production and testing of the LAr calorimeter support table. We wish to thank Claude Ferrari, Pierre Gimenez, Yves Bonnet, Denis Gacon and Alain Pinget of CERN EN/MEF group for the continuous mechanical support provided in the CERN SPS North Are during the installation of the setup and the data taking. This work was supported in part by the European Community, through the ARTEMIS Research Training Network (Contract number MRTN-CT-2006-035657) and by GRICES and FCT, Portugal.

## References

- [1] S. Gadomski, et al., Deployment and use of the ATLAS DAQ in the combined test beam, ATL-DAQ-CONF-2005-019, ATL-COM-DAQ-2005-014, CERN, 2005.
- [2] T. Sjöstrand, S. Mrenna, P. Skands, JHEP 05 (2006) 026.
- [3] S. Agostinelli, et al., Meth. Phys. Res. A 506 (2003) 250; J. Allison, et al., IEE Trans. Nucl. Sci. NS-53 (1) (2006) 270.
- [4] D. Costanzo, ATLAS detector simulation: status and outlook, ATL-SOFT-PUB-2005-004, CERN-ATL-SOFT-PUB-2005-004, ATL-COM-SOFT-2005-008, 2005.
- [5] I. Efthymiopoulos, A. Fabich, The very low 1–9 GeV/c tertiary beam extension of the H8 beam line of CERN SPS, CERN-AB-2005-036, 2005.
- [6] L. Gatignon, XCET: threshold Cerenkov counters (<http://ab-div-atb-ea.web.cern.ch/ab-div-atb-ea/documentation/eqpmts/xcet.html>).
- [7] J. Spanggaard, CERN SL, Note 98-023-BI.
- [8] B. Di Girolamo, A. Dotti, V. Giangiobbe, P. Johansson, L. Pribyl, M. Volpi, Beamline instrumentation in the 2004 combined ATLAS testbeam, ATL-TECH-PUB-2005-001, 2005.
- [9] ATLAS/Inner Detector Collaboration, Inner detector Technical Design Report, vol. I CERN/LHCC 97-016, vol. II CERN/LHCC 97-17, 1997.
- [10] ATLAS/Liquid Argon Calorimeter Collaboration, Liquid Argon Calorimeter Technical Design Report, CERN/LHCC 96-041, 1996.
- [11] ATLAS/Tile Calorimeter Collaboration, Tile Calorimeter Technical Design Report, CERN/LHCC 96-042, 1996.
- [12] ATLAS/Muon Spectrometer Collaboration, Muon spectrometer Technical Design Report, CERN/LHCC 97-022, 1997.
- [13] P. Adragna, et al., Nucl. Instr. and Meth. A (2009), doi:10.1016/j.nima.2009.04.009.
- [14] G. Aad, et al., J. Instr. 3 (2008) S08003.
- [15] E. Bergeås, S. Hellman, K. Jon-And, Very low energy muons in ATLAS TileCal, ATL-TILECAL-PUB-2005-001, CERN, 2005.
- [16] M. Aleksa, et al., ATLAS combined testbeam: computation and validation of the electronic calibration constants for the electromagnetic calorimeter, ATL-LARG-PUB-2006-003, 2006.
- [17] M. Aharrouché, et al., Performance of the liquid argon electromagnetic ATLAS calorimeter measured at 2004 ATLAS combined testbeam, in preparation.